

## RESEARCH ARTICLE

WILEY

# A mesh-independent method for planar three-dimensional crack growth in finite domains

A. Sheng<sup>1</sup>  | N. M. Ghoniem<sup>1</sup> | T. Crosby<sup>2</sup> | G. Po<sup>1</sup>

<sup>1</sup>Department of Mechanical and Aerospace Engineering, University of California, Los Angeles, California

<sup>2</sup>Alberta Innovates Technology Futures, Edmonton, Alberta, Canada

## Correspondence

Andrew Sheng, Department of Mechanical and Aerospace Engineering, University of California, Los Angeles, CA 90095-1597.  
Email: asheng@g.ucla.edu

## Funding information

Air Force Office of Scientific Research (AFOSR), Grant/Award Number: FA9550-16-1-0444; US Department of Energy, Grant/Award Number: DE-SC0018410; National Science Foundation, Division of Civil, Mechanical and Manufacturing Innovation (CMMI), Grant/Award Number: 1563427

## Summary

The discrete crack mechanics (DCM) method is a dislocation-based crack modeling technique where cracks are constructed using Volterra dislocation loops. The method allows for the natural introduction of displacement discontinuities, avoiding numerically expensive techniques. Mesh dependence in existing computational modeling of crack growth is eliminated by utilizing a superposition procedure. The elastic field of cracks in finite bodies is separated into two parts: the infinite-medium solution of discrete dislocations and an finite element method solution of a correction problem that satisfies external boundary conditions. In the DCM, a crack is represented by a dislocation array with a fixed outer loop determining the crack tip position encompassing additional concentric loops free to expand or contract. Solving for the equilibrium positions of the inner loops gives the crack shape and stress field. The equation of motion governing the crack tip is developed for quasi-static growth problems. Convergence and accuracy of the DCM method are verified with two- and three-dimensional problems with well-known solutions. Crack growth is simulated under load and displacement (rotation) control. In the latter case, a semicircular surface crack in a bent prismatic beam is shown to change shape as it propagates inward, stopping as the imposed rotation is accommodated.

## KEYWORDS

dislocations, finite element methods, fracture, solids

## 1 | INTRODUCTION

Fracture is a complicated process that depends strongly on factors such as loading conditions, geometry, and material properties. Cracks are seldom loaded in the traditional modes (opening, sliding, and tearing) separately and generally have three-dimensional (3D) character. Despite many efforts in the field of fracture mechanics, most realizations are two-dimensional (2D), and threshold material properties (eg, fracture toughness) are usually measured under plane strain conditions. Progress in fracture mechanics of truly 3D cracks of complex shapes has been slow, even though experimental observations strongly suggest that cracks generally possess 3D characters. Additionally, when cracks grow, practical calculations of the elastic field around propagating cracks can be a real challenge. These numerical difficulties stem from one fundamental fact: most current numerical techniques try to satisfy boundary conditions of the elastic field at the crack tip, although it is known to have an essential singularity. It is therefore desirable to have the ability to predict the behavior

of 3D cracks of arbitrary shapes under complex loading conditions in a manner that is not sensitive to the discretization details (ie, mesh size) close to a propagating crack.

We present here a fracture modeling technique, henceforth referred to as the discrete crack mechanics (DCM) method, as a mesh-independent alternative to existing numerical methods for modeling propagating cracks in linear elastic materials. Cracks are represented in DCM by distributions of discrete Volterra dislocations, dubbed “crack dislocations” to differentiate them from crystal dislocations associated with plasticity. Crack dislocations remain free of the material constraints that confine crystal dislocations to certain slip planes and Burgers vectors. Instead, the orientations and Burgers vectors of crack dislocations are determined by the crack geometry and loading conditions.

The similarities between the stress fields near a crack tip and a pileup of dislocations against a fixed dislocation were first observed by Eshelby et al.<sup>1</sup> Their work provides a solution for the dislocation distribution that gives an accurate crack tip stress field approximation for a single-crack tip in 2D. Weertman presents the dislocation distributions for more complete cases of 2D cracks in elastic and elastic-plastic materials in his comprehensive book *Dislocation-based Fracture Mechanics*.<sup>2</sup> The solutions, obtained using Hilbert transforms, are given for linear 2D cracks in all three loading modes, with both single-crack tips (edge cracks) and double-crack tips (embedded cracks). In contrast to the techniques used in these works, the dislocation distributions representing cracks are obtained numerically in the DCM method for cracks of arbitrary shape under arbitrary loading in both 2D and 3D.

At its core, much of DCM is based on the parametric dislocation dynamics (PDD) method first developed by Ghoniem et al.<sup>3</sup> and expands on variational principles utilized by Po and Ghoniem.<sup>4</sup> The elastic field of 3D cracks was shown to be obtained accurately using dislocation arrays by Ghoniem and Huang.<sup>5</sup> Subsequently, Takahashi and Ghoniem showed that the stress intensity factor (SIF) at the crack tip could also be obtained from the dislocation-based crack model and applied the technique to simulate a number of crack problems, including a special case of a mixed-mode crack as well as fatigue crack propagation according to the Paris law.<sup>6</sup> The present investigation builds upon these works by establishing the conditions required for the dislocation representation of generalized mixed-mode cracks. Additionally, a variational formulation of the equation of motion governing the crack tip during critical crack growth is derived, and its use in simulating stable and unstable crack growth in finite elastic bodies is demonstrated.

Our focus in this work is on quasi-static (slowly moving cracks) for which inertial dynamic effects are negligible because their speed is much smaller than the speed of sound in the material. The stress field of dynamic cracks has been studied using various analytical and computational methods.<sup>7–9</sup> As for a dislocation-based method, there is potential for simulating dynamic crack growth by considering the elastodynamic fields of fast-moving dislocations. For this, the author would refer the audience to the work of Cui et al, in which the explicit solutions for dislocation movement under high strain rates and their numerical implementation are provided.<sup>10</sup> The main objective here is to show that 3D slowly propagating interior and surface cracks can be modeled, independent of an underlying mesh in the body, and without remeshing as the crack moves. In achieving this goal, we first develop the theoretical foundations of the method and then validate its numerical accuracy and convergence by comparing to known solutions in 2D and 3D. We finally demonstrate the numerical procedure in the study of an interior 3D crack and a surface crack, both slowly propagating under external loading. While bulk crack simulations have been conducted using dislocation-based models,<sup>5,6</sup> the surface crack example shown in this work is the first known dislocation-based model of a growing surface crack.

Two main features will be apparent in modeling cracks using the DCM method, the first being that the crack representation in DCM is highly mesh insensitive, as compared to techniques such as the element erosion or interelement separation techniques that suffer from a high degree of mesh dependence due to the fact that cracks can only exist along element boundaries.<sup>11</sup> To combat the issue of mesh structure dependence, meshless methods have been developed in which a solution approximation is obtained not by interpolation across mesh elements as in finite element-based methods but rather through the use of nodes only.<sup>12,13</sup> The element-free Galerkin method (EFGM) developed by Belytschko et al has been shown to be particularly effective for solving linear elastic fracture mechanics problems.<sup>14,15</sup> Its first application to 3D fracture can be found in the work of Sukumar et al who used the EFGM in the vicinity of a crack coupled with the finite element method (FEM) to model the remainder of the problem.<sup>16</sup> Krysl and Belytschko subsequently developed a technique for simulating crack growth using the EFGM.<sup>17</sup> Meshless methods utilizing local enrichment techniques have also been introduced, such as the method presented by Rabczuk and Belytschko to model complex crack branching problems.<sup>18</sup> While meshless methods provide several advantages over finite element-based methods including the elimination of crack path dependence on the mesh structure, there are still some notable disadvantages. Perhaps the simplest though nontrivial drawback to meshless methods is that they cannot be implemented into the existing finite element software that remains widely used in industry. This has motivated the development of partition of unity-based FEMs, such as the eXtended FEM (XFEM) and the Generalized FEM (GFEM).<sup>19–21</sup>

At their core, XFEM and GFEM are essentially the same method. That is, the partition-of-unity concept is used to introduce local “enrichment” functions allowing effects such as the displacement discontinuity of a crack to be captured by the introduction of a few additional degrees of freedom to the finite element approximation.<sup>22–24</sup> In its original formulation, the XFEM requires elements to be small compared to the crack size—a potential issue when considering small-scale cracking. This is because the crack tip enrichment functions, which are based on Westergaard’s near-tip solution, are extended beyond their valid range in cases where the crack size is similar to the element size. Several modifications to remedy this issue have since been proposed for the standard XFEM. Included is the work of Bellec and Dolbow who introduced ramped enrichment functions to limit the range of the standard crack tip enrichment functions to much success for 2D mixed-mode cracks in uniformly loaded square plates.<sup>25</sup> Rannou et al proposed a localized multigrid approach that ensured a fine enough mesh to properly enrich the nodal support of a crack. In this method, the initial discretization of the geometry is refined locally at the crack tips with a hierarchy of increasingly fine meshes. The field is approximated in the fine mesh using an iterative method efficient at smoothing the high-frequency error of the solution. The field approximation is then transferred to the next mesh in the hierarchy, and the error is again smoothed on this coarser mesh. Mesh refinement occurs by splitting the existing elements in each successive mesh, such that the initial discretization can be maintained during crack growth.<sup>26</sup>

In DCM, the total elastic field of a cracked body is segregated into two coupled problems, whose solutions are superimposed to give the total crack field. The first involves computing the strong localized crack field in an infinite medium using available analytical Green’s functions. The second problem involves a boundary value problem to ensure the conditions imposed on the boundaries of the elastic body are satisfied. Here, only the standard FEM is required with no localized mesh refinement necessary. Hence, DCM can be easily combined with existing FEM implementations. The superposition strategy is discussed in further detail in Section 2.3, where the insensitivity of crack growth and shape to the underlying mesh in finite domains is established. The reasons for such insensitivity are also uncovered.

Another feature of DCM is the ability to account for crack-crack and, simultaneously, crack-crystal dislocation interaction. Gracie and Belytschko achieved the same coupling by combining the XFEM with localized atomistic models in 2D models.<sup>27</sup> In their method, atomistic models are applied in regions near crack tips and crystal dislocations and their resulting discontinuities introduced into a continuum model by the XFEM nodal enrichment scheme. In DCM, cracks and crystal dislocations are represented with discrete Volterra dislocations, and their interactions follow naturally from the available Green’s functions for dislocations in infinite elastic media. Thus, the interactions between large numbers of dislocations can be computed quickly, which opens the door for direct coupling between fracture and crystal plasticity and the ability to simulate complex damage processes. Although the examples presented in this work focus only on elastic fracture, a variational formulation of DCM in conjunction with discrete crystal plasticity is presented in Section 3. It will be shown that the unified formulation produces the same configurational force that is responsible for the motion of crack tips (J-integral) and crystal dislocations (Peach-Koehler [PK] force) and that the equations of motion governing both types of defects are identical.

This paper is organized as follows. The foundational framework behind DCM is presented in Section 2, which covers the basic concept behind DCM through the derivation of the equations of motion governing slow crack growth. Its numerical implementation is discussed in Section 4. To confirm the validity of the DCM method, various 2D and 3D benchmarking examples are given in Section 5. In Section 6, several examples are given of quasi-static crack growth. First, the growth of a penny-shaped crack in a cylinder under a fixed tensile load is shown. The second example involves a penny-shaped crack in a rectangular prism under mode-I tensile loading, which illustrates the effect of free boundaries on crack growth. A beam bending problem makes for the final example in which a fixed rotation is applied to the ends of the beam, and the growth of a surface crack is shown to be arrested under such conditions.

## 2 | MODEL FORMULATION

The basic idea of DCM is illustrated in Figure 1 for a mode-I crack. Imagine a cut being made in a deformable stress-free material (gray) into which a rigid strip (red) of the same thickness as the Burgers vector is inserted. Now, make a cut in the strip and insert another shorter rigid strip (blue) with the same thickness. There is a displacement jump at the two ends of the shorter strip, shown as a smooth transition for illustrative purposes. This process continues until a desired crack opening distribution is created across the two cut surfaces. Note that the outer material boundary remains traction free, whereas the cut surfaces experience nonzero tractions. If a load is then applied to the outer boundary such that the tractions on the cut surfaces vanish, the inserted strips can now be removed, and the resulting elastic fields are equivalent to

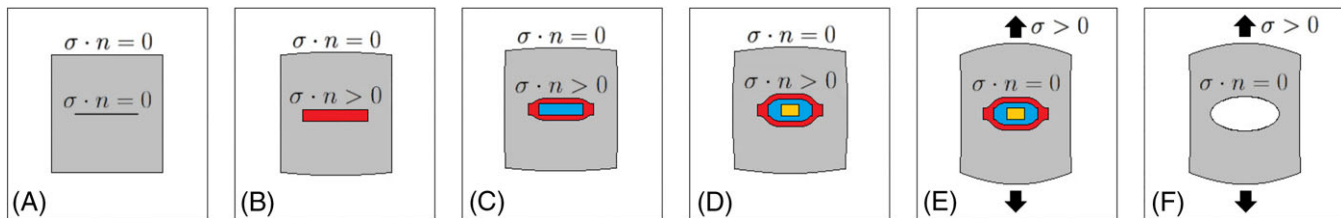


**FIGURE 1** Conceptual model of the Volterra dislocation representation of a mode-I crack [Colour figure can be viewed at [wileyonlinelibrary.com](http://wileyonlinelibrary.com)]

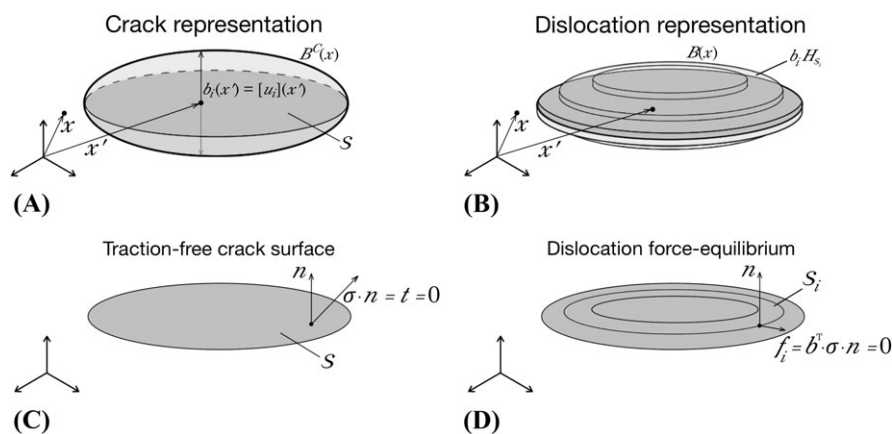


**FIGURE 2** A, Crack (Somigliana-type dislocation) spanning the surface  $S$ ; B, Stepped approximation; C, Traction-free crack surface condition; D, Force equilibrium condition on dislocation loops

that of a similarly sized crack under the same load. This cut-insert-relax process of forming the crack is actually mediated by an array of Volterra edge dislocation loops along the crack plane against a fixed outer loop, with their Burgers vectors oriented perpendicular to the crack surface. We will numerically mimic this conceptual process in our development of the method. The fixed outer loop, henceforth referred to as the leading dislocation, defines the crack tip. The leading dislocation is held fixed until the force (PK configurational force) exerted on it by the enclosed or trailing dislocations reaches a critical value at which point crack growth is initiated by advancing the leading dislocation. It will be shown in Section 3 that this force is equivalent to the J-integral along a crack tip.

## 2.1 | Three-dimensional dislocation-based representation of cracks

With reference to Figure 2, let us consider a crack surface  $S$  with displacement jump  $[u](\mathbf{x}')$  defined for every point  $\mathbf{x}'$  in  $S$ . The displacement jump of the crack can be described by a Somigliana dislocation having Burgers vector  $\mathbf{b}^C(\mathbf{x}') = [u](\mathbf{x}')$ . The crack opening displacement (COD) is then described by the field

$$\mathbf{B}^C(\mathbf{x}) = \int_S \mathbf{b}^C(\mathbf{x}') \delta(\mathbf{x} - \mathbf{x}') dA', \quad (1)$$

where  $\delta$  is the Dirac  $\delta$  function. As first noted by Eshelby,<sup>28</sup> the Somigliana dislocation can be approximated by an array of  $N$  Volterra dislocation loops, adequately arranged to collectively make up a stepped Somigliana dislocation. In DCM, this observation is utilized to construct a stepped approximation  $\mathbf{B}(\mathbf{x})$  of  $\mathbf{B}^C(\mathbf{x})$  using discrete Volterra dislocations as building blocks. Letting  $\mathbf{b}_i$  be the (constant) Burgers vector of the  $i$ th loop, the COD of the crack is then approximated by the stepped function

$$\mathbf{B}(\mathbf{x}) = \sum_{i=1}^N \mathbf{b}_i H_{S_i}(\mathbf{x} - \mathbf{x}'), \quad (2)$$

where  $H_{S_i}$  is the Heaviside step function defined on concentric partitions  $S_i$  of the original crack surface  $S$ .

Unlike dislocations however, forces cannot be transferred across crack surfaces because cracks are generally traction free, with the exception of pressurized cracks. Therefore, in order to correctly represent a crack, the dislocation distribution must satisfy the traction-free condition on the crack plane  $S$ . It will now be shown that a requirement equivalent to the traction-free condition is that a suitable array of dislocations be in force equilibrium. To this end, let us consider again the crack surface  $\int$  in Figure 2C. The traction on the crack surface must satisfy

$$\mathbf{t} = \boldsymbol{\sigma} \cdot \mathbf{n} = \mathbf{0}. \quad (3)$$

We now imagine representing the crack with an array of dislocation loops, each with Burgers vector  $\mathbf{b}$  lying within the surface  $S$ , as shown in Figure 2D. The force per unit length exerted on an elementary line element  $d\mathbf{l}$  of a dislocation by the stress field is the PK force, ie,

$$d\mathbf{f} = \boldsymbol{\sigma} \cdot \mathbf{b} \times d\mathbf{l}. \quad (4)$$

The component of this force on the crack plane is

$$d\mathbf{f}_{//} = \boldsymbol{\sigma} \cdot \mathbf{b} \times d\mathbf{l} - [(\boldsymbol{\sigma} \cdot \mathbf{b} \times d\mathbf{l}) \cdot \mathbf{n}] \mathbf{n} = (\mathbf{b}^T \cdot \boldsymbol{\sigma} \cdot \mathbf{n}) (\mathbf{n} \times d\mathbf{l}). \quad (5)$$

Because the dislocation array is restricted to move on the crack plane in the dislocation representation of cracks, the condition of mechanical equilibrium for these dislocations is

$$\mathbf{b}^T \cdot \boldsymbol{\sigma} \cdot \mathbf{n} = \mathbf{b}^T \cdot \mathbf{t} = 0. \quad (6)$$

Note that the dislocation equilibrium condition  $\mathbf{b}^T \cdot \mathbf{t} = 0$  is a weaker requirement than the traction-free condition  $\mathbf{t} = \mathbf{0}$ . However, if, instead of one array of dislocations with a constant Burgers vector, we use three arrays of dislocations with linearly independent Burgers vectors  $\mathbf{b}_1$ ,  $\mathbf{b}_2$ , and  $\mathbf{b}_3$ , respectively, then the equilibrium condition for the three sets becomes

$$\mathbf{B}^T \cdot \mathbf{t} = 0, \quad (7)$$

where  $\mathbf{B} = [\mathbf{b}_1, \mathbf{b}_2, \mathbf{b}_3]$  is the column matrix of the Burgers vectors of the three loop arrays. Because  $\mathbf{B}$  is nonsingular by construction, then the loop equilibrium condition (7) and the traction-free condition (3) are equivalent. In general, therefore, in DCM, each crack is represented by three sets of dislocation arrays with mutually orthogonal Burgers vectors so that a generic stress state can be annihilated on the crack surface by reaching the mechanical equilibrium of the dislocation arrays on the crack surface  $S$ . In Figure 3, the three sets are labeled A, B, and C. Set A consists of prismatic loops with their Burgers vectors orthogonal to the crack plane, whereas sets B and C consist of shear loops with their Burgers vectors lying on the crack plane. The leading dislocations in each set represent the crack tip and, therefore, must be coincident.

The system of dislocations can be equilibrated quasi-statically until an equilibrium configuration is achieved where the in-plane component of the PK force acting on each trailing dislocation vanishes, and therefore, the traction-free condition is satisfied along the dislocation lines in the crack surface. Note that in between dislocations, the traction-free condition is satisfied only approximately. Therefore, in order to improve numerical accuracy, one has to increase the number  $N$  of dislocations, such that Equation (7) becomes a closer approximation of Equation (3). However, we shall show in the following sections that the overall properties of the crack, such as the SIF, the COD, or even the stress field a short distance away from the crack surface, may be adequately obtained with only a few Volterra dislocations, and thus,  $N$  does not necessarily have to be very large. Moreover, it is understood that in Equations (3) to (7), the stress  $\boldsymbol{\sigma}$  is a superposition of

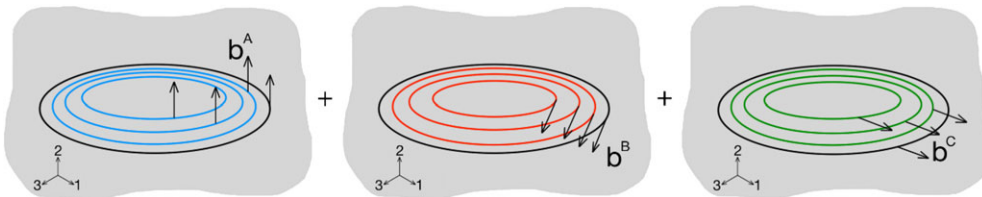


**FIGURE 3** Superposition of three sets of crack dislocation arrays gives the solution for a crack under general loading. The black leading dislocation loop in each set represents the crack tip



the dislocation and applied stresses  $\sigma^d$  and  $\sigma^a$ , respectively. The displacement and stress fields of a dislocation ensemble consisting of  $N_{\text{loop}}$  dislocation loops are given by<sup>29</sup>

$$u_i^d(\mathbf{x}) = \sum_{\gamma=1}^{N_{\text{loop}}} \left\{ -\frac{b_i \Omega(\mathbf{x})}{4\pi} + \frac{1}{8\pi} \oint_C \left[ \epsilon_{ikl} b_l R_{,pp} + \frac{1}{1-\nu} \epsilon_{kmn} b_n R_{,mi} \right] dl'_k \right\}, \quad (8)$$

$$\sigma_{ij}^d(\mathbf{x}) = \frac{\mu b_n}{4\pi} \sum_{\gamma=1}^{N_{\text{loop}}} \left\{ \oint_C \left[ \frac{1}{2} R_{,mpp} (\epsilon_{kmn} dl'_i + \epsilon_{imn} dl'_j) + \frac{1}{1-\nu} \epsilon_{jmn} (R_{,ijm} - \delta_{ij} R_{,ppm}) dl'_k \right] \right\}. \quad (9)$$

Here,  $\mu$  and  $\nu$  are the shear modulus and Poisson's ratio of the material,  $\mathbf{b}$  is the dislocation Burgers vector,  $\mathbf{R} = \mathbf{x} - \mathbf{x}'$ , and the contour integrals on the  $\mathbf{x}'$  variable are evaluated along the dislocation loop denoted by  $C$ . Moreover,  $\Omega(\mathbf{x})$  is the solid angle subtended by the dislocation loop at the field point. Discrete forms of the elastic field of multiple-loop ensembles based on Equations (8) and (9) were developed by Ghoniem and Sun as an ingredient in the PDD method, in which loops are divided into segments of parametric space curves.<sup>30</sup> Numerical quadrature is then used to perform the integration on each segment. The elastic fields described by expressions (8) and (9) account for both the interaction between separate dislocation loops and the self-interaction of a dislocation loop.

## 2.2 | DCM in 2D

For 2D problems (eg, plane stress or strain), we consider infinitely long dislocation loops represented as dislocation dipoles, as shown in Figure 4. Consider a 2D mode-I crack of length  $2a$  under a uniform applied stress  $\sigma_{yy}^a$ . The crack lies along the  $x$ -axis and is represented by a continuously distributed displacement jump  $\mathbf{B}(x)$  (Somigliana dislocation). The stress field on the crack plane is the sum of the dislocation stress and the applied stress, as follows:

$$\sigma_{yy}(\mathbf{x}) = \frac{\mu}{2\pi(1-\nu)} \int_{-a}^a \frac{\mathbf{B}(x')}{x-x'} dx' + \sigma_{yy}^a(x), \quad \{x | -a \leq x \leq a\}. \quad (10)$$

The traction-free condition along the crack line can be expressed as a balance of the stress resulting from a distribution of infinitely long and straight edge dislocations in an isotropic material<sup>29</sup> and the applied stress  $\sigma_{yy}^a$ , ie,

$$\sigma_{yy}(\mathbf{x}) = 0, \quad \{x | -a \leq x \leq a\}, \quad (11)$$

where  $\mu$  is the shear modulus and  $\nu$  is Poisson's ratio. An approximation of Equation (11) can be obtained by replacing the distributed displacement jump with  $N$  discrete Volterra dislocations having Burgers vectors  $b_j$  and the integral with a summation over the dislocations, ie,

$$\frac{\mu}{2\pi(1-\nu)} \sum_{j=1(j \neq i)}^N \frac{b_j}{x_i - x_j} + \sigma_{yy}^a(x_i) = 0. \quad (12)$$

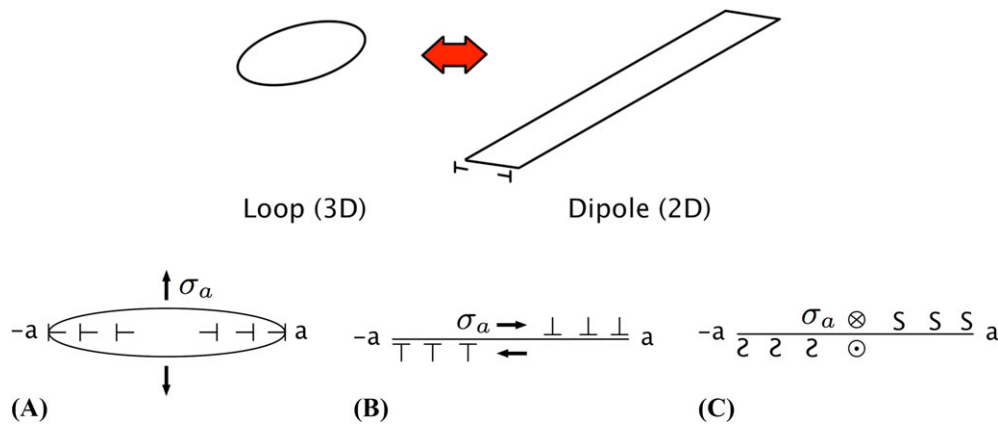


**FIGURE 4** Three-dimensional (3D) crack loops and two-dimensional (2D) crack dipoles and a 2D representation of a (A) mode-I crack, (B) mode-II crack, and (C) mode-III crack [Colour figure can be viewed at [wileyonlinelibrary.com](http://wileyonlinelibrary.com)]

The first term gives the stress on a crack dislocation located at  $x_i$  due to the presence of a dislocation located at  $x_j$ . This stress must balance out the applied stress  $\sigma_{yy}^a$  felt by dislocation  $i$  to satisfy the traction-free condition at  $x_i$ .

Equivalently, if Equation (12) is multiplied by the Burgers vector of the  $i$ th dislocation  $b_i$ , a balance of the PK force in the crack plane is satisfied for each dislocation, with the exception of the leading dislocations. For a mode-I crack represented by dislocations with Burgers vectors along the  $y$ -direction and line sense vectors along the  $z$ -direction, the PK forces on each dislocation are given by

$$\begin{aligned} f_x^{(i)} &= \frac{\mu b_i}{2\pi(1-\nu)} \sum_{j=1(j \neq i)}^N \frac{b_j}{x_i - x_j} + \sigma_{yy}^a b_i = 0 \\ f_y^{(i)} &= f_z^{(i)} = 0. \end{aligned} \quad (13)$$

Similarly, mode-II cracks can be represented by edge dislocations oriented with their Burgers vectors parallel to the crack surface and along the shearing direction. Mode-III cracks can be represented by pileups of screw dislocations lying on the crack plane with Burgers vectors parallel to the shearing direction. Two-dimensional crack representations are shown in Figure 4.

It has been previously shown that a mixed mode-II/mode-III crack can be modeled using only a single set of crack dislocations.<sup>6</sup> However, this is only valid under the special case considered. For a more general example, let us consider a simple 2D configuration where a crack on the plane  $x_2 = 0$  is represented by two arrays of dislocations  $A$  and  $B$  aligned with the  $x_1$  direction and having linearly independent Burgers vectors in the crack plane. Suppose that the crack is loaded under combined modes II and III by applied shear stresses  $\tau_{12}^a$  and  $\tau_{23}^a$ . The traction-free condition on the crack plane is given by

$$\boldsymbol{\sigma} \cdot \mathbf{n} = \begin{bmatrix} 0 & \tau_{12} & 0 \\ \tau_{12} & 0 & \tau_{23} \\ 0 & \tau_{23} & 0 \end{bmatrix} \cdot \begin{bmatrix} 0 \\ 1 \\ 0 \end{bmatrix} = \begin{bmatrix} \tau_{12} \\ 0 \\ \tau_{23} \end{bmatrix} = 0, \quad (14)$$

where the shear stresses  $\tau_{ij}$  consist of the dislocation and applied stresses. On the other hand, the stresses result in the in-plane PK forces that must be equilibrated, ie,

$$\begin{bmatrix} f^A \\ f^B \end{bmatrix} = \begin{bmatrix} b_1^A & 0 \\ 0 & b_2^B \end{bmatrix} \cdot \begin{bmatrix} \tau_{12} \\ \tau_{23} \end{bmatrix} = 0. \quad (15)$$

Since the Burgers vectors of the two dislocation arrays are linearly independent, the traction must be zero for the dislocations to be in equilibrium.

### 2.3 | Coupling DCM with FEM for cracks in finite geometries

The presence of boundaries gives rise to an additional component of the configurational force on each crack dislocation. This additional component, known as the image force, is present whenever the dislocation is confined in a finite domain  $\Omega$ .<sup>28</sup> The effect of the image force is accounted for by utilizing a superposition-based method, described first by Eshelby<sup>28</sup> and numerically implemented by Van der Giessen and Needleman.<sup>31</sup> This procedure separates the computation of the full dislocation fields in the finite domain  $\Omega$  into two parts. In the first, the dislocation fields  $\boldsymbol{\sigma}^d$  and  $\mathbf{u}^d$  in an infinite domain are calculated using Equations (8) and (9). From this solution, the tractions and displacements on a virtual boundary  $\mathcal{S}^v$  that is equivalent to the boundary  $\partial\Omega$  are calculated for use in the second part. The second part, which has the express purpose of correcting the infinite-domain solution to satisfy the boundary conditions on  $\partial\Omega$ , will henceforth be referred to as the correction problem. It consists of a boundary value problem of which the displacement field solution  $\mathbf{u}^c$  must satisfy the following conditions:

$$\begin{cases} \sigma_{ij}^c = C_{ijkl} u_{k,l}^c & \text{in } \Omega \\ \sigma_{ij,j}^c = 0 & \text{in } \Omega \\ \sigma_{ij}^c \hat{n}_j = t_i^a - \sigma_{ij}^d \hat{n}_j & \text{on } \partial\Omega^t \\ u_i^c = u_i^a - u_i^d & \text{on } \partial\Omega^u, \end{cases} \quad (16)$$

where  $C_{ijkl}$  is the stiffness tensor,  $\sigma_{ij}^c$  is the correction stress,  $\hat{n}_j$  is the outward surface normal on  $\partial\Omega$ ,  $\partial\Omega^t$  is the boundary on which Neumann conditions are specified, and  $\partial\Omega^u$  is the boundary on which Dirichlet conditions are specified. Note that in the correction problem, the total traction applied on  $\partial\Omega^t$  has two components, the first being the applied traction

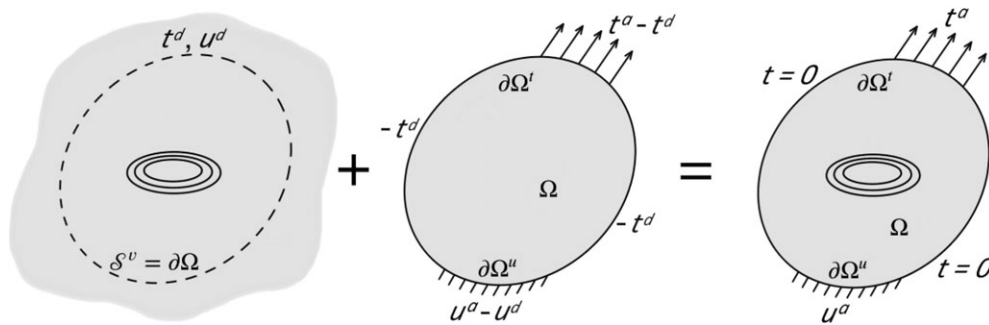


**FIGURE 5** Superposition method for a mode-I crack in a finite domain. Summing up the infinite-medium dislocation array field and the correction boundary value problem gives the dislocation array field in a finite body

$t_i^a$  and the second being the *reversed* dislocation traction  $-\sigma_{ij}^d \hat{n}_j$  from the infinite-medium solution. Similarly, the total prescribed displacement on  $\partial\Omega^u$  is comprised of the prescribed displacement  $u_i^a$  and the *reversed* dislocation displacement  $-u_i^d$  from the infinite-medium solution.

To solve for  $\mathbf{u}^c$ , we take the weak form of the third line of Equation (16) written in vector notation and multiply by a test function  $\tilde{\mathbf{u}}$ , ie,

$$\int_{\Omega} \nabla \tilde{\mathbf{u}}^T \mathbf{C} \nabla \mathbf{u}^c dV = \int_{\partial\Omega} \tilde{\mathbf{u}}^T (\mathbf{t}^a - \sigma^d \hat{\mathbf{n}}) dA. \quad (17)$$

The standard Galerkin finite element procedure then renders a discrete system of equations for the nodal displacements  $\mathbf{U}$  of the form

$$\mathbf{K}\mathbf{U} = \mathbf{F} - \mathbf{F}^d, \quad (18)$$

where  $\mathbf{K}$  is the global stiffness matrix,  $\mathbf{U}$  is the vector of nodal degrees of freedom,  $\mathbf{F}$  is the global force vector due to external loads, and  $\mathbf{F}^d$  is the image force vector due to the internal dislocation loops. The correction problem solution can then be obtained by solving Equation (18). Superimposing the infinite-medium and correction problem solutions gives the corrected elastic field of the dislocation array, as illustrated in Figure 5.

The advantage of this procedure becomes apparent in problems involving crack growth. Because there is no need to introduce the crack discontinuity into the correction problem, the solution may be computed using the standard FEM procedure. The only knowledge required for the FEM correction problem is on the boundary tractions and displacements from the dislocation array. These can be computed quickly since the dislocation array solution is known from Equations (8) and (9). This eliminates the need to remesh as the dislocation array expands during crack growth, since only the reversed tractions applied in the boundary value problem need to be recalculated from the infinite-medium solution. Additionally, since the near-tip field is calculated apart from the correction problem, mesh refinement is unnecessary in the correction part of the solution. Two examples are given in Section 6 that illustrate the effect of the correction problem.

In practice, another challenge arises when a portion of a crack dislocation lies on a virtual boundary. Specifically, it becomes numerically challenging to compute Equation (9) along the boundary—a necessary step for the boundary correction problem. To resolve this issue, we exploit the fact that Equation (16) does not restrict the distribution of dislocations to be inside the boundary.<sup>32</sup> Therefore, an arbitrary dislocation loop can be placed outside of the boundary such that a section coincides with the boundary dislocation as shown in Figure 6. If the Burgers vector of the external “virtual” dislocation is the same as the crack dislocation and its line sense vector points in the opposite direction, the fields of the overlapping sections cancel each other out. Computing Equation (9) is therefore avoided for the boundary segments. While the infinite medium and correction fields are dependent on the virtual dislocations, the total solution is unaffected by them.<sup>32</sup> An example of a surface crack, which necessarily contains dislocation segments along a boundary, is shown in Section 6.3.

### 3 | IRREVERSIBLE THERMODYNAMICS OF QUASI-STATIC CRACK GROWTH

The J-integral and the PK force both describe the configurational force (change in energy with respect to a change in defect shape or position) that drives crack propagation and dislocation motion, respectively. Eshelby's energy momentum tensor serves as the basis for the general force on a defect, of which the J-integral and PK force are special cases. Integrating the



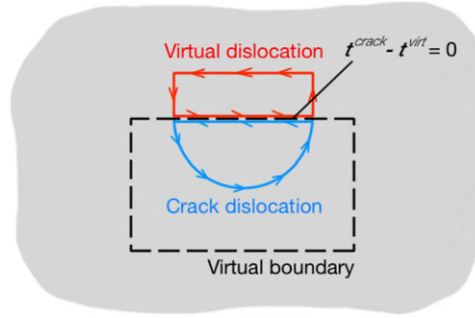


**FIGURE 6** Illustration of a virtual dislocation loop used to cancel the field from a boundary crack dislocation segment. Note the line sense vectors along the boundary point in opposite directions [Colour figure can be viewed at [wileyonlinelibrary.com](http://wileyonlinelibrary.com)]

divergence of the energy momentum tensor over a body of volume  $V$  bounded by a surface of area  $A$  and applying the divergence theorem, we have

$$\int_V (W\delta_{ij} - \sigma_{jk}\beta_{ki}^E)_{,j} dV = \int_{\partial V} (W\delta_{ij} - \sigma_{jk}\beta_{ki}^E) n_j dA. \quad (19)$$

If one dimension is constant, as is the case with prismatic structures, the integral reduces to

$$f_i = L \oint_{\Gamma} (W\delta_{ij} - \sigma_{jk}\beta_{ki}^E) n_j d\Gamma, \quad (20)$$

where  $f_i$  is the configurational force acting on a defect enclosed by the contour  $\Gamma$ . Within the framework of compatible elasticity, the elastic distortion tensor  $\beta_{ki}^E$  and the displacement gradient  $u_{k,i}$  are equal, giving the definition of the 2D J-integral as follows:

$$J_i = \frac{f_i}{L} = \int_{\Gamma} (W\delta_{ij} - \sigma_{jk}u_{k,i}) n_j d\Gamma. \quad (21)$$

In 3D, a local J-integral can be calculated by evaluating Equation (21) for slices along a section of thickness  $L$  along the crack tip, as shown in Figure 7. A summation of these local J-integrals gives an approximation of the surface integral in Equation (19) over the section. Belytschko and Gracie recognized that the PK force could be calculated by evaluating the J-integral about a dislocation and used this approach when modeling dislocations with the XFEM.<sup>33</sup>

In contrast, by using Volterra dislocation “building blocks,” fracture mechanics can be reformulated within the framework of incompatible elasticity.<sup>32,34</sup> Within this framework, the displacement gradient is the sum of two separate tensors, the elastic deformation tensor  $\beta_{ki}^E$ , and the plastic deformation tensor  $\beta_{ki}^P$ . As a result, Equation (19) can be rewritten in terms of the dislocation density tensor  $\alpha_{km}$ , which is the curl of  $\beta_{ki}^P$ , ie,

$$\int_V (W\delta_{ij} - \sigma_{jk}\beta_{ki}^E)_{,j} dV = \int_V \sigma_{jk} (\beta_{ki,j}^P - \beta_{kj,i}^P) dV = \int_V \sigma_{jk}\epsilon_{ijm}\alpha_{km} dV. \quad (22)$$

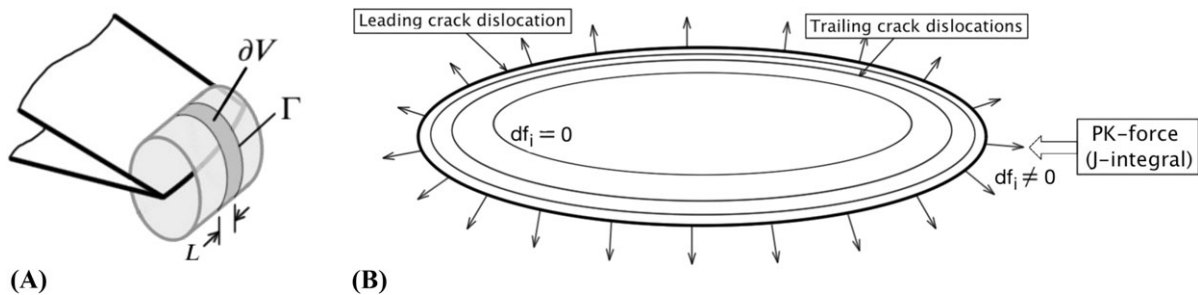


**FIGURE 7** A, Approximating the three-dimensional (3D) J-integral by evaluating slices along the crack tip; B, Conceptual diagram of a 3D J-integral on leading crack dislocation. The trailing dislocations are in equilibrium while the fixed leading dislocation has unbalanced Peach-Koehler (PK) forces acting along it that are equivalent to local J-integrals

Substituting the form of  $\alpha_{km}$  for Volterra dislocations with Burgers vector in the  $x_k$  direction and line tangent along the  $x_m$  direction, we have

$$\int_V \sigma_{jk} \epsilon_{ijm} \alpha_{km} dV = \int_V \sigma_{jk} \epsilon_{ijm} \left[ \oint \delta(\mathbf{x} - \mathbf{x}') b_k dl'_m \right] dV. \quad (23)$$

If we change the order of integration and apply the sifting property of the Dirac  $\delta$  function, the above equation reduces to a single integral, ie,

$$f_i = \oint \left[ \int_V \sigma_{jk} \delta(\mathbf{x} - \mathbf{x}') dV \right] \epsilon_{ijm} b_k dl'_m = \oint \epsilon_{ijm} \sigma_{jk} b_k dl_m, \quad (24)$$

where  $df_i = \epsilon_{ijm} \sigma_{jk} b_k dl_m$  is the PK force acting on a dislocation segment of infinitesimal length  $dl$ . If this force is zero, the segment is in equilibrium and does not need to move; otherwise, it will undergo dissipative motion in the direction of the force to minimize the elastic energy. The procedure we establish here aims at equilibrating all trailing dislocations by a “virtual” time-marching scheme. When the trailing dislocations are in equilibrium (ie, the PK forces acting on them are balanced), the J-integral of the crack in quasi-equilibrium can be obtained by evaluating Equation (24) to obtain the unbalanced PK force along the leading dislocation, as shown in Figure 7B.

The fracture toughness of a material corresponds to a critical PK resistance force on the leading dislocation. Once the J-integral rises above the critical PK force, the crack advances in a dissipative medium. When the onset of crack growth is detected, the leading dislocation (which is initially fixed for a static crack) is displaced according to an equation of motion that we develop here. Energy dissipation mechanisms are numerous in materials (point and extended defect formation, phonon drag, heat flows, etc) and will not be discussed further here. All these mechanisms can be lumped into an effective mobility (or viscosity) parameter  $B$ , which, for leading dislocations, may have a physical basis. For the trailing dislocations,  $B$  is a purely numerical quantity, which can be helpful in faster convergence of the solution.

The equation of motion that governs crack growth is obtained here using a variational approach, by which the internal entropy production rate is maximized subject to some physical constraints. This approach, which is based on the *principle of maximum rate of entropy production*, has been used to formulate the governing equations in discrete dislocation dynamics, coupled with vacancy and heat diffusion.<sup>4</sup> We extend the procedure here to the situation where cracks and crystal dislocations are both present.

The Clausius-Duhem statement for a body  $\Omega_0$  containing no other sources of internal entropy production aside from cracks and dislocations is given by

$$-\rho_0 \dot{\psi} + \sigma_{kj} v_{j,k} = \theta \pi \geq 0, \quad (25)$$

where  $\rho_0$  is the mass density per unit volume,  $\psi$  is the Helmholtz free energy density,  $\sigma_{jk}$  is the Cauchy stress tensor,  $v_{j,k}$  is the distortion rate,  $\theta$  is the absolute temperature, and  $\pi$  is the internal entropy production rate. The total displacement gradient or distortion  $u_{i,j}$  is taken to be

$$u_{i,j} = \beta_{ij}^E + \beta_{ij}^P + \beta_{ij}^C, \quad (26)$$

where  $\beta_{ij}^E$  is the elastic distortion tensor, and  $\beta_{ij}^P$  is the plastic distortion tensor of the form<sup>34</sup>

$$\beta_{ij}^P(\mathbf{x}, t) = \int_{S^P} b_i^P \delta(\mathbf{x} - \mathbf{x}') da'_j, \quad (27)$$

and similarly, the crack distortion tensor  $\beta_{ij}^C$  takes the form

$$\beta_{ij}^C(\mathbf{x}, t) = \int_{S^C} b_i^C(\mathbf{x}') \delta(\mathbf{x} - \mathbf{x}') da'_j. \quad (28)$$

Here, the surface bounded by the dislocation loop is denoted  $S^P$ , whereas the surface bounded by the crack tip line is denoted  $S^C$ . The crystal dislocation Burgers vector is denoted  $\mathbf{b}^P$ , and  $\mathbf{b}^C(\mathbf{x}')$  is the crack Burgers vector. The difference between  $\beta_{ij}^P$  and  $\beta_{ij}^C$  is that the crystal dislocation Burgers vector is constant, whereas the crack Burgers vector is a function of position  $\mathbf{x}'$  as described in Section 2. The material time derivative of Equation (26) gives the distortion rate to be

$$v_{i,j} = \dot{\beta}_{ij}^E + \dot{\beta}_{ij}^P + \dot{\beta}_{ij}^C. \quad (29)$$

Substituting Equation (29) into Equation (25) gives

$$-\rho_0 \dot{\psi} + \sigma_{kj} \left( \dot{\beta}_{jk}^E + \dot{\beta}_{jk}^P + \dot{\beta}_{jk}^C \right) = \theta \pi \geq 0. \quad (30)$$

If we take  $\psi$  to be of the form  $\psi(\mathbf{x}, t) \equiv \psi(\boldsymbol{\epsilon}^E)$ , where the elastic strain  $\boldsymbol{\epsilon}^E$  is the symmetric part of  $\boldsymbol{\beta}^E$ , then taking the material time derivative gives

$$\dot{\psi} = \frac{\partial \psi}{\partial \epsilon_{ij}^E} \dot{\epsilon}_{ij}^E.$$

The Clausius-Duhem statement can then be expanded into the form

$$-\rho_0 \frac{\partial \psi}{\partial \epsilon_{ij}^E} \dot{\epsilon}_{ij}^E + \sigma_{kj} \left( \dot{\beta}_{jk}^E + \dot{\beta}_{jk}^P + \dot{\beta}_{jk}^C \right) = \theta \pi \geq 0. \quad (31)$$

Because  $\sigma_{jk}$  is symmetric and its double inner product with the skew-symmetric part of  $\dot{\beta}_{jk}^E$  is zero, Equation (31) can be rewritten as

$$\left( -\rho_0 \frac{\partial \psi}{\partial \epsilon_{ij}^E} + \sigma_{ij} \right) \dot{\epsilon}_{ij}^E + \sigma_{ij} \dot{\beta}_{ij}^P + \sigma_{ij} \dot{\beta}_{ij}^C = \theta \pi \geq 0. \quad (32)$$

Since elastic deformation may be recovered, it does not contribute to internal entropy production, and thus, from the first term in Equation (32), we get the following constitutive equation:

$$\sigma_{ij} = \rho_0 \frac{\partial \psi}{\partial \epsilon_{ij}^E}. \quad (33)$$

The internal entropy production rate  $\pi$  may then be expressed as

$$\frac{\sigma_{ij}}{\theta} \dot{\beta}_{ij}^P + \frac{\sigma_{ij}}{\theta} \dot{\beta}_{ij}^C = \pi \geq 0. \quad (34)$$

All possible physical contributions to the rate of entropy production are contained on the left-hand side of Equation (32) as products of generalized forces and fluxes. For convenience, the left-hand side will be defined as

$$\phi \equiv \frac{\sigma_{ij}}{\theta} \dot{\beta}_{ij}^P + \frac{\sigma_{ij}}{\theta} \dot{\beta}_{ij}^C. \quad (35)$$

However, Equation (34) alone does not provide a means for uniquely identifying the relationships between the generalized forces and fluxes that govern how the system actually evolves. The principle of maximum rate of entropy production states that a physical system evolves in such a way as to maximize the rate of entropy production. By using Equation (34) to constrain the maximization of  $\pi$ , the coupled evolution equations governing a system that contains both cracks and dislocations can be obtained.

Using the method of Lagrange multipliers, the constrained  $\pi$  functional may be written as

$$\Pi = \int_{\Omega_0} [\pi + \lambda(\pi - \phi)] dV. \quad (36)$$

The functional  $\Pi$  is maximized when its variation is stationary for any arbitrary variation in its arguments. The value of the Lagrange multiplier  $\lambda$  is determined by  $\lambda = n/(1 - n)$ , where  $n$  is the order of  $\pi$  in the generalized fluxes. Take  $\pi$  to be a quadratic functional of  $\mathbf{w}^P$  and  $\mathbf{w}^C$ ,<sup>4</sup> then

$$\pi [\mathbf{w}^P, \mathbf{w}^C] = \oint_{L^P} \delta(\mathbf{x} - \mathbf{x}') B_{ij}^P w_i^P w_j^P dl' + \oint_{L^C} \delta(\mathbf{x} - \mathbf{x}') B_{ij}^C w_i^C w_j^C dl', \quad (37)$$

where the dislocation velocity  $\mathbf{w}^P$  and crack tip velocity  $\mathbf{w}^C$  are generalized irreversible fluxes contributing to  $\pi$ . The first and second terms correspond to energy dissipated by dislocation motion and crack growth, respectively. Substituting the

expressions for  $\phi$  and  $\pi$ , as well as the value of the Lagrange multiplier  $\lambda = -2$ , Equation (36) becomes

$$\Pi[\mathbf{w}^P, \mathbf{w}^C] = \int_{\Omega_0} \left[ \frac{2\sigma_{ij}}{\theta} \dot{\beta}_{ij}^P + \frac{2\sigma_{ij}}{\theta} \dot{\beta}_{ij}^C - \oint_{L^P} \delta(\mathbf{x} - \mathbf{x}') B_{ij}^P w_i^P w_j^P dl' - \oint_{L^C} \delta(\mathbf{x} - \mathbf{x}') B_{ij}^C w_i^C w_j^C dl' \right] dV. \quad (38)$$

The explicit form of  $\dot{\beta}_{ij}^P$  is given by<sup>34</sup>

$$\dot{\beta}_{ij}^P = \oint_{L^P} \delta(\mathbf{x} - \mathbf{x}') b_i^P \epsilon_{jkm} w_k^P dl'_m. \quad (39)$$

The explicit form of  $\dot{\beta}_{ij}^C$  is obtained by taking the time derivative of Equation (28) and applying the surface transport and divergence theorems.<sup>35</sup> By doing so, one obtains

$$\dot{\beta}_{ij}^C = \oint_{L^C} \delta(\mathbf{x} - \mathbf{x}') b_i^C(\mathbf{x}') \epsilon_{jkm} w_k^C dl'_m + \int_{S^C} \dot{b}_i^C(\mathbf{x}') \delta(\mathbf{x} - \mathbf{x}') da'_j, \quad (40)$$

where  $\mathbf{b}^P$  is the dislocation Burgers vector,  $\mathbf{b}^C$  is the crack tip Burgers vector, and  $\dot{\mathbf{b}}^C$  is a “crack opening displacement flux” vector. Then, Equation (38) becomes

$$\begin{aligned} \Pi[\mathbf{w}^P, \mathbf{w}^C, \dot{\mathbf{b}}^C] = \int_{\Omega_0} \left\{ \frac{2\sigma_{ij}}{\theta} \int_{S^C} \dot{b}_i^C(\mathbf{x}') \delta(\mathbf{x} - \mathbf{x}') da'_j + \frac{2\sigma_{ij}}{\theta} \oint_{L^C} \delta(\mathbf{x} - \mathbf{x}') b_i^C \epsilon_{jkm} w_k^C dl'_m \right. \\ \left. - \int_{L^C} \delta(\mathbf{x} - \mathbf{x}') B_{ij}^C w_i^C w_j^C dl' + \frac{2\sigma_{ij}}{\theta} \oint_{L^P} \delta(\mathbf{x} - \mathbf{x}') b_i^P \epsilon_{jkm} w_k^P dl'_m - \oint_{L^P} \delta(\mathbf{x} - \mathbf{x}') B_{ij}^P w_i^P w_j^P dl' \right\} dV \end{aligned} \quad (41)$$

Using the sifting property of the Dirac  $\delta$  function, the functional  $\Pi$  may be rewritten as

$$\begin{aligned} \Pi[\mathbf{w}^P, \mathbf{w}^C, \dot{\mathbf{b}}^C] = \int_{S^C} \frac{2\sigma_{ij}}{\theta} \dot{b}_i^C n_j da + \oint_{L^C} \left[ \frac{2\sigma_{ij}}{\theta} (b_i^C \epsilon_{jkm} w_k^C \hat{\xi}_m) - B_{ij}^C w_i^C w_j^C \right] dl \\ + \oint_{L^P} \left[ \frac{2\sigma_{ij}}{\theta} b_i^P \epsilon_{jkm} w_k^P \hat{\xi}_m - B_{ij}^P w_i^P w_j^P \right] dl. \end{aligned} \quad (42)$$

Taking the variation of  $\Pi$  with respect to the generalized fluxes and imposing stationarity, we have

$$\begin{aligned} \delta\Pi = \int_{S^C} \left( \frac{\sigma_{ij}}{\theta} n_j \right) \delta b_i^C da + \oint_{L^C} \left( \frac{1}{\theta} \epsilon_{ijk} \sigma_{jm} b_m^C \hat{\xi}_k - B_{ij}^C w_j^C \right) \delta w_i^C dl \\ + \oint_{L^P} \left[ \frac{1}{\theta} \epsilon_{ijk} \sigma_{jm} b_m^P \hat{\xi}_k - B_{ij}^P w_j^P \right] \delta w_i^P dl = 0. \end{aligned} \quad (43)$$

The evolution equations of the system are obtained as a result of the constrained maximization. From the first term, we obtain the traction-free crack surface condition

$$\sigma_{ij} n_j = 0. \quad (44)$$

The second term gives a mobility equation for crack dislocations with a configurational force term identical to that of the PK force that acts on crystal dislocations, ie,

$$\frac{1}{\theta} \epsilon_{ijk} \sigma_{jm} b_m^C \hat{\xi}_k = B_{ij}^C w_j^C. \quad (45)$$

The third term gives the mobility equation with the familiar PK configurational force per unit dislocation length, as follows:

$$\frac{1}{\theta} \epsilon_{ijk} \sigma_{jm} b_m^P \hat{\xi}_k = B_{ij}^P w_j^P. \quad (46)$$

## 4 | NUMERICAL IMPLEMENTATION

Discrete dislocation dynamics simulations have evolved as a powerful tool for the simulation of the equilibrium configurations of dislocation ensembles.<sup>3,4</sup> We follow here a similar procedure for a system of cracks and dislocations for the numerical implementation of the equations of motion. In Equation (43), the first and second terms govern the evolution of the crack. The first term imposes the traction-free crack surface condition, namely,  $\frac{1}{\theta}\sigma_{ij}n_j = 0$ , on crack surface  $S^C$ . The second term determines the motion of the crack tip  $L^C$ . In the PDD method,<sup>3</sup> dislocation lines are represented by uniform cubic or quintic Hermite splines that preserve the continuity of the tangent vector at the spline vertices, referred to herein as dislocation nodes. Hermite-type degrees of freedom can be ascribed to each node  $\alpha$ : a position vector  $\mathbf{p}_\alpha$  and a tangent vector  $\mathbf{t}_\alpha$ . A dislocation segment  $(\alpha, \beta)$  is then associated with a cubic spline  $\mathbf{r}_\alpha^\beta$  given in component form by (with  $u \in [0, 1]$ )

$$\begin{aligned} \mathbf{r}_\alpha^\beta(u) &= [1 \ u \ u^2 \ u^3] \begin{bmatrix} 0 & 0 & 1 & 0 \\ 0 & 0 & 0 & \gamma_{\alpha\beta} \\ 3 & -\gamma_{\alpha\beta} & -3 & -2\gamma_{\alpha\beta} \\ -2 & \gamma_{\alpha\beta} & 2 & \gamma_{\alpha\beta} \end{bmatrix} \begin{bmatrix} p_{\beta i} \\ t_{\beta i} \\ p_{\alpha i} \\ t_{\alpha i} \end{bmatrix} \\ &= [H_1 \ H_2 \ H_3 \ H_4] \cdot [p_{\beta i} \ t_{\beta i} \ p_{\alpha i} \ t_{\alpha i}]^T, \end{aligned} \quad (47)$$

where  $\gamma_{\alpha\beta}$  is the parametric chord length of the spline. The vector form of (47) is given by

$$\begin{aligned} \mathbf{r}_\alpha^\beta(u) &= [IH_1 \ IH_2 \ IH_3 \ IH_4] \cdot [\mathbf{p}_\beta^T \ \mathbf{t}_\beta^T \ \mathbf{p}_\alpha^T \ \mathbf{t}_\alpha^T]^T \\ &= \mathbf{H}(u) \cdot \mathbf{h}_\alpha^\beta. \end{aligned} \quad (48)$$

Replacing the closed line integrals in Equation (43) into fast sums,<sup>30</sup> we obtain

$$\sum_{(\alpha,\beta) \in \mathcal{G}_C} \int_\alpha^\beta [\delta \mathbf{w}^{CT} (\mathbf{B}^C \mathbf{w}^C - \mathbf{f}^C)] dl + \sum_{(\alpha,\beta) \in \mathcal{G}_P} \int_\alpha^\beta [\delta \mathbf{w}^{PT} (\mathbf{B}^P \mathbf{w}^P - \mathbf{f}^P)] dl = 0. \quad (49)$$

Taking the time derivative of Equation (48) and substituting (48) in (49), the following discrete system is obtained:

$$\sum_{(\alpha,\beta) \in \mathcal{G}_C} [\delta \dot{\mathbf{h}}_\alpha^{\beta T} (\mathbf{K}_{\alpha\beta}^C \dot{\mathbf{h}}_\alpha^\beta - \mathbf{f}_\alpha^C)]_C + \sum_{(\alpha,\beta) \in \mathcal{G}_P} [\delta \dot{\mathbf{h}}_\alpha^{\beta T} (\mathbf{K}_{\alpha\beta}^P \dot{\mathbf{h}}_\alpha^\beta - \mathbf{f}_\alpha^P)]_P = 0, \quad (50)$$

where the first term in the sum is for crack nodes and the second sum is for dislocation nodes. The segment stiffness matrices  $\mathbf{K}_{\alpha\beta}$  and force vector  $\mathbf{f}_\alpha^\beta$  have been obtained as

$$\mathbf{K}_{\alpha\beta} = \int_0^1 \mathbf{H}^T \mathbf{B} \mathbf{H} J du \quad \mathbf{f}_\alpha^\beta = \int_0^1 \mathbf{H}^T \mathbf{f} J du \quad (51)$$

with the Jacobian  $J = \frac{dl}{du} = \left| \frac{\partial \mathbf{r}_\alpha^\beta}{\partial u} \right|$ . Since the variations in nodal degrees of freedom  $\delta \dot{\mathbf{h}}_\alpha^{\beta T}$  are arbitrary, the equations of motion for crack and dislocation nodes can be obtained in the form

$$(\mathbf{K}_{\alpha\beta}^C \dot{\mathbf{h}}_\alpha^\beta - \mathbf{f}_\alpha^C)_C = 0 \quad (\mathbf{K}_{\alpha\beta}^P \dot{\mathbf{h}}_\alpha^\beta - \mathbf{f}_\alpha^P)_P = 0. \quad (52)$$

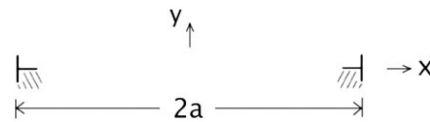
The system of Equations (52) can be readily assembled in global matrices, and a set of linear ordinary differential equations is obtained following procedures established in the FEM.<sup>3,4</sup> Since we are interested here in crack growth without crystal dislocations, we describe in the following our procedure to initiate the shape of the crack, select the appropriate Burgers vector, and solve the equations of motion.

The algorithm used to determine the equilibrium configuration of the crack dislocations is summarized in Table 1. In 2D, a pair of fixed dislocations separated by a distance equal to the crack length describes the total length of the crack. In 3D, a dislocation loop defines the shape of the crack. A dislocation dipole or loop free to expand or contract along the crack plane is placed inside the fixed dislocation, and the entire system is allowed to equilibrate. The distance by which a dislocation node is extended is based on a specified maximum displacement  $dx_{\max}$  per crack growth step. The PK force on a dislocation node is calculated, and the velocity is obtained through the relationship in Equation (52). A maximum



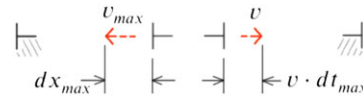
**TABLE 1** The crack dislocation equilibrium algorithm

1. Initialize crack by placing a fixed dipole a distance of  $2a$  apart, where  $a$  is the half-crack width.



2. Insert a trailing dipole and calculate  $v$  for each dislocation according to Equation (52).

Compute  $dt_{\max} = dx_{\max}/v_{\max}$ , where  $v_{\max}$  is the largest calculated velocity. Move each dislocation by  $v \cdot dt_{\max}$ .



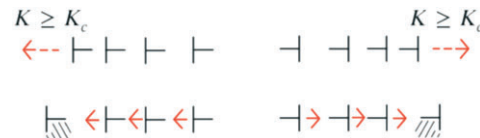
3. Once the trailing dipole is in equilibrium, insert a new trailing dipole and follow the same procedure in step 2 to find the new equilibrium configuration.



4. The crack representation is obtained when the current dislocation configuration is in equilibrium and the applied load can no longer sustain additional trailing dislocations.



5. If the stress intensity factor  $K$  at the fixed leading dislocations (crack tip) exceed the fracture toughness  $K_c$ , advance the leading dislocations according to Equation (52) and follow repeat steps 2-5 to find the new crack configuration.



simulation time step  $dt_{\max}$  is then calculated based on the specified  $dx_{\max}$  and the maximum dislocation node velocity  $v_{\max}$ . All trailing dislocation nodes are then moved by a distance given by the product of  $dt_{\max}$  and the velocity  $v$  calculated for each dislocation node. Once the free dislocations have reached their equilibrium positions, a new dipole or dislocation loop is seeded inside the previous one, and the system is again allowed to equilibrate. The process is repeated until the applied load is no longer sufficient to support any additional dislocations. Once the final crack shape is found, the SIF  $K$  along the fixed dislocation is calculated. If it exceeds the fracture toughness  $K_c$ , the crack tip dislocation is advanced according to Equation (52). For growing cracks,  $dx_{\max}$  can be updated at each crack growth step to improve the solution time for the equilibrium positions of the trailing dislocations. The amount by which  $dx_{\max}$  is changed is dependent on the crack size—as the crack grows larger,  $dx_{\max}$  should be increased proportionally. In the examples that follow, the specified maximum displacements used are approximately  $dx_{\max} \approx a/2000$ .

To obtain values of the number of dislocation loops and the Burgers vector to represent a given crack, we utilize an analytical estimate for a single crack in an infinite medium. The displacement in the case of a 2D crack of length  $2a$  in an infinite medium under a mode-I load is

$$u^+(x_1, 0) - u^-(x_1, 0) = 2\sigma \left( \frac{1-\nu}{\mu} \right) \sqrt{a^2 - x_1^2}, \quad (53)$$

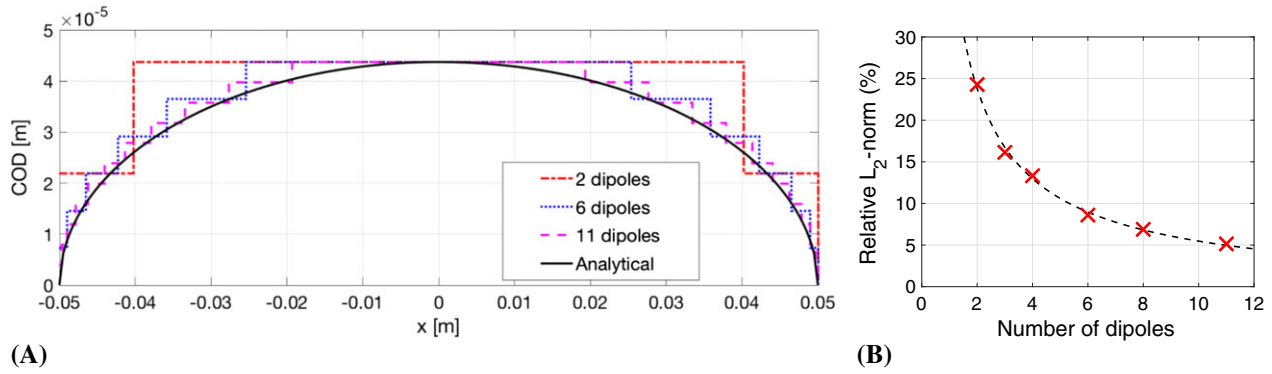


**FIGURE 8** A, Upper crack surface opening displacement (COD) vs  $x$  for 2, 6, and 11 dislocation dipole representations; B, Relative  $L_2$ -norm (%) vs number of dipoles [Colour figure can be viewed at [wileyonlinelibrary.com](http://wileyonlinelibrary.com)]

where the (+) and (−) superscripts denote the displacements of the upper and lower crack surfaces, respectively. Evaluated at  $x_1 = 0$ , the above expression gives the COD at the crack center,<sup>36</sup> as follows:

$$\text{COD} = 2\sigma a \left( \frac{1-\nu}{\mu} \right). \quad (54)$$

The COD given by the dislocation-based crack model is the product of  $N$ , the number of dipoles for 2D problems or dislocation loops for 3D problems, and the Burgers vector:  $\text{COD} = Nb$ . In general, the COD cannot be determined a priori in a complex stress field, and in such cases, an estimate for a reasonable Burgers vector must be made. If we choose  $N$  to be large enough (we will show that  $N \geq 5$  is sufficient), an approximation may be obtained for the Burgers vector of Volterra dislocations as

$$Nb \approx \frac{2\bar{\sigma}a(1-\nu)}{\mu}, \quad (55)$$

where  $N$  is an estimate of the number of dipoles to be used in the crack model,  $b$  is the approximate Burgers vector magnitude, and  $\bar{\sigma}$  is the average stress along the crack line. If we now scale the Burgers vector by the crack length ( $2a$ ) and the stress by the shear modulus, ie,  $\tilde{b} = b/2a$ , and  $\tilde{\sigma} = \frac{\sigma(1-\nu)}{\mu}$ , we obtain a very simple way to estimate the Burgers vector, as follows:

$$\tilde{b} \approx \frac{\tilde{\sigma}}{N}. \quad (56)$$

The scaled stress here is estimated from the far field, which, in practice, is at a distance of 2–3 times the crack size, or the remote applied stress in simple problems. A similar approximation can be obtained for cracks in 3D by considering the opening displacement at the center of a mode-I penny-shaped crack, which is approximately half that of the 2D mode-I crack,<sup>36</sup> ie,

$$\text{COD} = 4\sigma a \left( \frac{1-\nu}{\pi\mu} \right). \quad (57)$$

The Burgers vector approximation is then obtained from the following relationship:

$$Nb \approx \frac{4\bar{\sigma}a(1-\nu)}{\pi\mu}. \quad (58)$$

Note that the crack shape can be approximated by adding one Burgers vector at each dislocation starting at the outermost fixed pair. As the number of dislocations is increased, the decreasing length of the Burgers vector leads to better resolution of the crack profile. This is illustrated in Figure 8A, which includes the analytical COD solution given by Equation (53) and the COD relative  $L_2$ -norm.

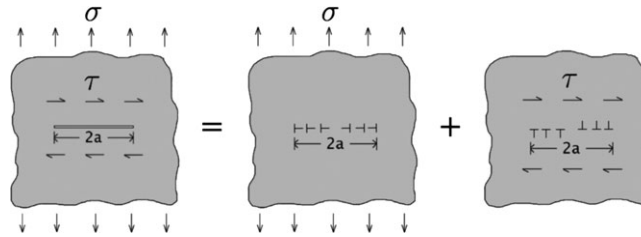


**FIGURE 9** Decomposition of a mixed-mode crack

## 5 | BENCHMARKING OF THE NUMERICAL ACCURACY

### 5.1 | Two-dimensional cracks in infinite domains

Now that we have an approximate method to select the Burgers vector, we need to determine its orientation with respect to the loading direction under mixed-mode conditions. We show here that the superposition principle of linear elasticity holds and that independent families of crack dislocations can effectively represent a general crack under mixed-mode loading, by decomposing it into two separate cracks under mode-I and mode-II loadings, respectively. Each crack can be represented by a family of dislocations, as shown in Figure 9. The positions of the dislocations in both families must be such that the traction-free boundary condition on the crack surfaces is satisfied. That is, the following must result from the positions of the dislocations:

$$\sigma \cdot n = \begin{bmatrix} \sigma_{11} & \tau_{12} & 0 \\ \tau_{21} & \sigma_{22} & 0 \\ 0 & 0 & 0 \end{bmatrix} \cdot \begin{bmatrix} 0 \\ 1 \\ 0 \end{bmatrix} = \begin{bmatrix} \tau_{12} \\ \sigma_{22} \\ 0 \end{bmatrix} = 0. \quad (59)$$

Using the PK formula, the forces acting on the dislocations in each family are found to be

$$\begin{bmatrix} f_1 \\ f_2 \\ f_3 \end{bmatrix}_I = \begin{bmatrix} \sigma_{11} & \tau_{12} & \tau_{13} \\ \tau_{21} & \sigma_{22} & \tau_{23} \\ \tau_{31} & \tau_{32} & \sigma_{33} \end{bmatrix} \cdot \begin{bmatrix} 0 \\ b_2 \\ 0 \end{bmatrix}_I \times \begin{bmatrix} 0 \\ 0 \\ 1 \end{bmatrix}_I = \begin{bmatrix} \sigma_{22} \cdot b_2 \\ \tau_{12} \cdot b_2 \\ 0 \end{bmatrix}_I \quad (60)$$

$$\begin{bmatrix} f_1 \\ f_2 \\ f_3 \end{bmatrix}_{II} = \begin{bmatrix} \sigma_{11} & \tau_{12} & \tau_{13} \\ \tau_{21} & \sigma_{22} & \tau_{23} \\ \tau_{31} & \tau_{32} & \sigma_{33} \end{bmatrix} \cdot \begin{bmatrix} b_1 \\ 0 \\ 0 \end{bmatrix}_{II} \times \begin{bmatrix} 0 \\ 0 \\ 1 \end{bmatrix}_{II} = \begin{bmatrix} \tau_{21} \cdot b_1 \\ \sigma_{11} \cdot b_1 \\ 0 \end{bmatrix}_{II}, \quad (61)$$

where Equations (60) and (61) show the force components acting on the mode-I and mode-II crack dislocations, respectively. Recall that crack dislocations are constrained to move only in the crack plane. That is, the edge dislocations of mode-I move by climb, whereas those representing mode-II move by glide. Thus, for mode-I, the equilibrated force is  $f_1 = \sigma_{22}b_2$ . Exactly on the crack plane (ie,  $x_2 = 0$ ), the set of glide dislocations of mode-II has  $\sigma_{22} = 0$ , and hence, they do not affect the motion of mode-I dislocations. In a similar manner, for mode-II dislocations,  $f_1 = \tau_{12}b_1$ , and since the climb dislocations of mode-I have  $\tau_{12} = 0$  on the crack plane,<sup>29</sup> they do not influence the motion of mode-II dislocations. With this scenario, we can run simultaneous simulations of both dislocation systems completely independently of one another. The same procedure can be extended to mode-III cracks, where screw dislocations would be needed. This separation into three independent sets of dislocations, two edge and one screw, a crack of arbitrary complexity can be represented. As we will see in the next section, 3D cracks are represented with prismatic loops (edge) for mode-I and shear loops (glide) for modes II and III.

Analytical formulas are available for the SIFs of a crack of length  $2a$ , inclined at an angle  $\beta$  from the loading axis. The values of  $K_I$  and  $K_{II}$ , calculated using the DCM method for slanted cracks oriented at an angle  $\beta$ , are compared in Figure 10 to the analytical SIF given in the work of Rooke and Cartwright,<sup>37</sup> ie,

$$K_I = \sqrt{\pi a} (\sigma_{22} \cos^2 \beta + \sigma_{11} \sin^2 \beta) \quad (62)$$

$$K_{II} = \sqrt{\pi a} (\sigma_{22} - \sigma_{11}) \sin \beta \cos \beta. \quad (63)$$

A remote stress of 60 MPa along the  $x_1$ -direction and 100 MPa along the  $x_2$ -direction is applied to a generic sample (shear modulus of  $\mu = 80$  MPa and Poisson's ratio of  $\nu = 0.3$ ). Each crack of half-crack length  $a = 0.03$  m is represented with six dislocation dipoles, with Burgers vectors ranging from 5.28 to 8.75  $\mu\text{m}$  for the mode-I component and from 0.30 to 1.75  $\mu\text{m}$  for the mode-II component. However, even with six dislocation dipoles, the agreement between the numerical results and the analytical formulas is excellent, as can be seen in Figure 10.

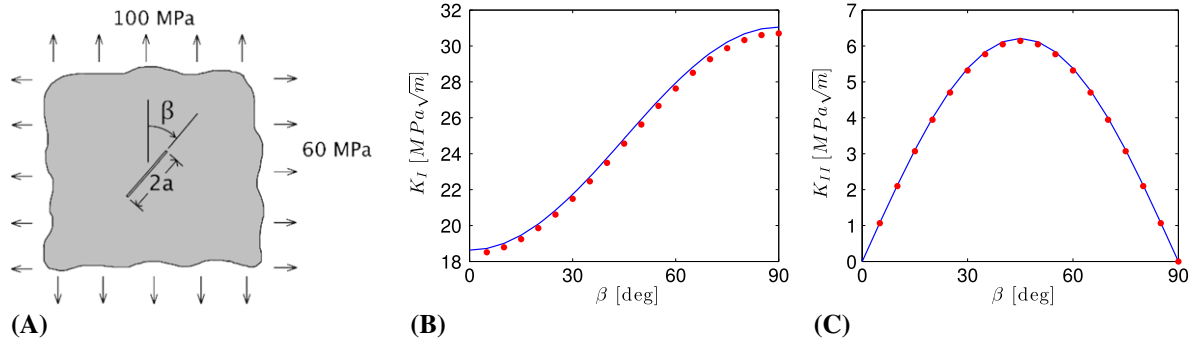


**FIGURE 10** (A) A mixed-mode crack in an infinite plate. The stress intensity factor is plotted against the crack orientation  $\beta$  for (B) mode-I and (C) mode-II. Red dots indicate the discrete crack mechanics numerical solution, and the solid blue line is the analytical solution<sup>37</sup>

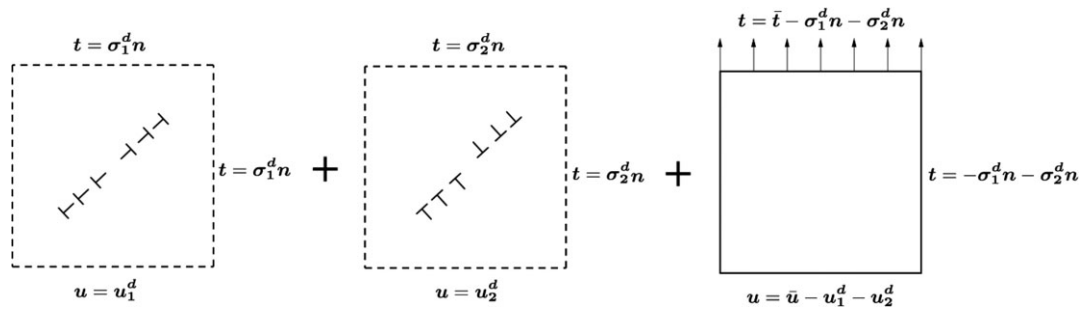


**FIGURE 11** Coupling of the mode-I and mode-II components of a mixed-mode crack in the boundary correction problem

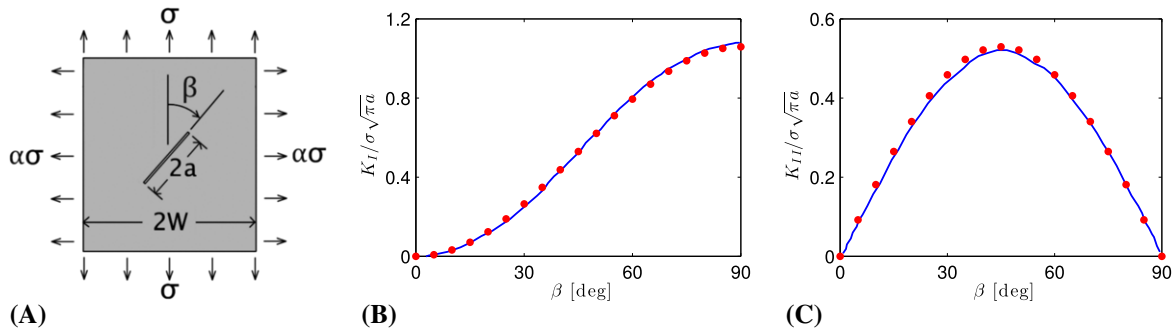


**FIGURE 12** (A) A mixed-mode crack in a finite plate. The shape factor is plotted against the crack orientation  $\beta$  for (B) mode-I and (C) mode-II. Red dots indicate the discrete crack mechanics numerical solution, whereas the solid blue line is given by Hammouda et al<sup>38</sup>

## 5.2 | Two-dimensional cracks in finite domains

When cracks exist in finite domains, however, the complete independence between mode-I and mode-II dislocations should be examined. The field of an inclined crack in a finite domain can also be decomposed into separate mode-I and mode-II problems. Since we utilize the solutions of the elastic fields of dislocations in an infinite medium, the two sets of dislocations would not directly exert force on one another. However, coupling of the two problems takes place once we add the boundary correction problem, which is illustrated in Figure 11. This can be a weak coupling, as long as the boundaries are far from the two dislocation sets. This situation is fortunate, because the strong dislocation-dislocation interaction field is avoided between the two sets of dislocations, and only their indirect effects show up in forces resulting from the boundary correction field. In Figure 12, the SIF for mode-I and mode-II families of dislocations calculated using the DCM method are compared to those given by Hammouda et al<sup>38</sup> for a series of inclined cracks in a square plate. The plate material has an elastic modulus of  $E = 206$  GPa and a Poisson's ratio of  $\nu = 0.3$ . The half-crack length to plate-width

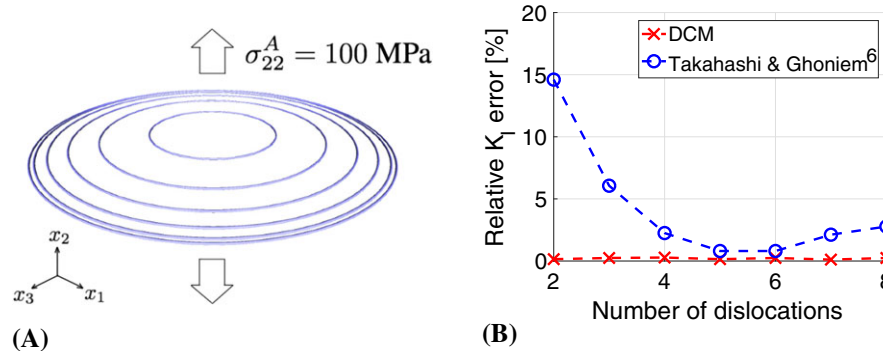


**FIGURE 13** A, Displacement contours of a penny-shaped crack under pure mode-I loading; B, Relative error in  $K_I$  of the mode-I penny-shaped crack in an infinite domain as a function of the number of dislocation loops. DCM, discrete crack mechanics [Colour figure can be viewed at [wileyonlinelibrary.com](http://wileyonlinelibrary.com)]

ratio used is  $a/W = 0.3$ , and the remote applied stress is  $\sigma = 100$  MPa along the  $x_2$  direction only. The number of dipoles used for each crack model ranges from six to eight, giving excellent agreement with their calculations.

### 5.3 | Three-dimensional cracks in infinite domains

The penny-shaped crack in an infinite body is a classic 3D crack problem with a well-known analytical solution given by<sup>36</sup>

$$K_I = 2\sigma \sqrt{\frac{a}{\pi}}. \quad (64)$$

In this example, a penny-shaped crack of diameter  $2a = 1 \mu\text{m}$  in an infinite medium is subjected to a uniform 100-MPa tensile load in the mode-I direction, as seen in Figure 13A. DCM simulations are performed using arrays consisting of two to eight dislocation loops. The Burgers vectors are chosen according to Equation (58) and range from 0.07 nm for an eight-dislocation array to 0.28 nm for a two-dislocation array. The relative SIF ( $K_I$ ) error plotted against the number of dislocations in each simulation is shown in Figure 13B. Takahashi and Ghoniem modeled the same penny crack problem in their implementation of the dislocation-based crack model in which the Burgers vector was chosen arbitrarily.<sup>6</sup> Their simulations have been repeated here with the same number of dislocations and corresponding Burgers vectors, which range from 0.08 nm for a six-dislocation array to 0.14 nm for a two-dislocation array. Figure 13B shows that even just a two-dislocation representation of the crack results in a surprisingly low error of roughly 15% in  $K_I$ . However, the relative  $K_I$  error is greatly reduced by using the Burger's vector approximation method described in Section 4. Note that while the SIF can be obtained with only a few dislocations, the COD is better represented when more dislocations are used, as shown in Figure 8B.

## 6 | QUASI-STATIC CRACK GROWTH

To demonstrate the utility of the mesh-independent method in studies of crack growth without remeshing as the crack advances, we consider three different crack problems. The first is an axisymmetric problem that demonstrates unstable crack growth under a fixed load. In this example, the SIF computed with the correction problem is compared to the solution when the correction problem is not included. In the second case, a penny-shaped crack in a rectangular prism is shown to grow preferentially along the minor axes toward the nearer surfaces, illustrating the boundary effect on the crack shape. To demonstrate stable crack growth, a fixed rotation is applied to a rectangular prism containing a thumbnail crack at its surface. This case is similar to the study presented in the work of Moës et al.,<sup>19</sup> where crack growth without remeshing is demonstrated. However, one must know where the crack is in relation to the underlying mesh to ensure proper enrichment shape functions. Here, in our third example, there is no relationship between the crack position and the underlying mesh. The first two cases are “load control,” whereas the last is “displacement control.”

### 6.1 | Axisymmetric crack growth under load control

Under a fixed applied load, otherwise referred to as a “dead load,” crack growth is unstable as  $K$  increases with crack extension. In the following example, a uniform prescribed traction of 90 MPa is applied to the upper surface of a boron



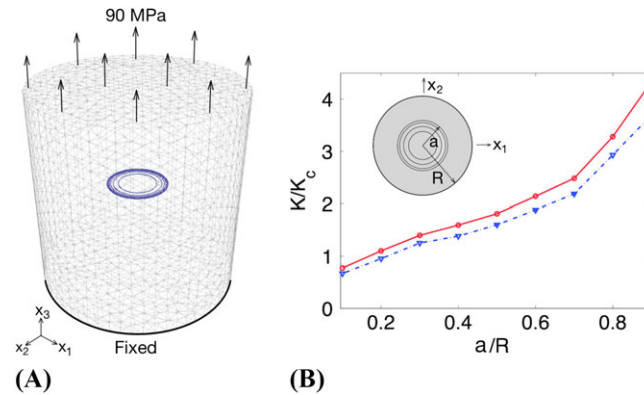


**FIGURE 14** A, Loading conditions on the cylinder containing a penny-shaped crack; B,  $K/K_c$  vs  $a/R$  for an applied traction of 90 MPa on a boron nitride cylinder of 4-mm radius and 8-mm height, containing a penny-shaped crack of initial radius 0.4 mm. The load is increased gradually to a critical value of 90 MPa and then held constant. The solid curve corresponds to the applied, dislocation interaction, and correction stresses on the crack, whereas the dashed line is without the correction problem contribution [Colour figure can be viewed at [wileyonlinelibrary.com](http://wileyonlinelibrary.com)]

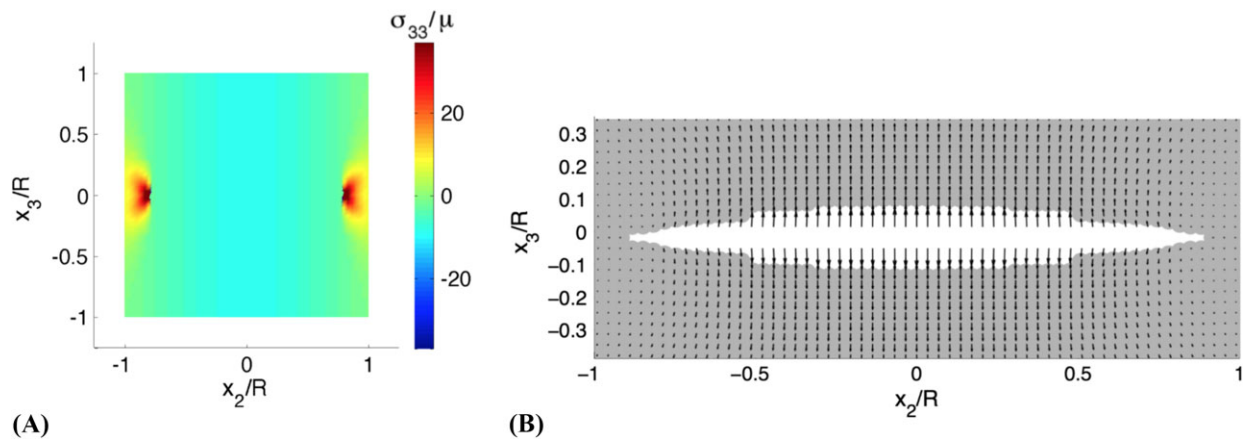


**FIGURE 15** A,  $\sigma_{33}/\mu$  field when  $r/R = 0.8$ ; B, Close-up of the crack opening when  $r/R = 0.8$ . The arrows show the displacement field in the crack vicinity

nitride (BN) cylinder ( $\mu = 18.5$  GPa,  $\nu = 0.27$ ,  $K_c = 2.5$  MPa $\sqrt{\text{m}}$ ), whereas the lower surface is held fixed. The cylinder has a height of 8 mm and a radius of  $R = 4$  mm and contains a penny crack with an initial radius of  $a_0 = 0.4$  mm, as shown in Figure 14A. The applied traction is gradually increased from zero until  $K > K_c$  on the leading dislocation loop and then held constant at 90 MPa. Figure 14B shows that under this constant load, the SIF increases as the crack grows toward the outer surface. The ratio of  $K/K_c$  is shown to increase significantly as the crack approaches the outer surface. The effect of the “image force” from the surface (the FEM part of the solution due to corrections of boundary tractions) is shown to be negligible during most of the crack history. It is surprising to see that even for a crack that is 90% the size of the cylinder diameter, the correction is only about 15%.

Figure 15A shows one component of the stress field  $\sigma_{33}$  in the cylinder when the crack is near the outer surface ( $r/R = 0.8$ ). The stress field is nearly the same as the applied stress ( $\sigma_{\text{applied}}/\mu = 0.00486$ ) everywhere, except for the zone between the crack tip and the surface. The corresponding displacement field around the crack is shown in a close-up view in Figure 15B. Note that due to the discrete representation of the crack with Volterra dislocations, there is a displacement jump at each location of a crack dislocation loop.

## 6.2 | Preferential crack growth due to boundary correction effects

In the following example, a prescribed displacement of  $6.384$   $\mu\text{m}$  is applied to the upper surface of a  $2.5$  mm  $\times$   $1$  mm  $\times$   $3$  mm rectangular prism with its bottom surface held fixed. The prism contains a penny crack with an initial radius of  $a_0 = 0.2$  mm, as shown in Figure 16A. The prism, which is comprised of BN, has a fracture toughness of  $K_c = 2.5$  MPa $\sqrt{\text{m}}$ .

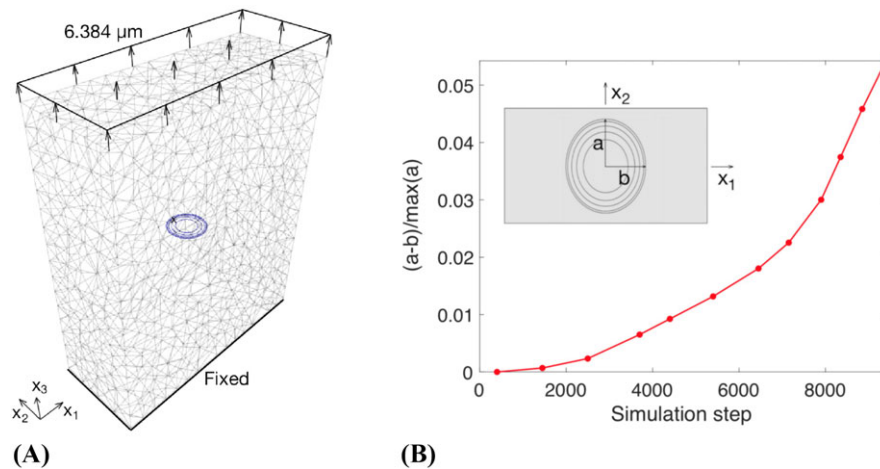


**FIGURE 16** A, Loading conditions on the rectangular prism containing a penny crack; B, Difference between the major and minor dimensions of a penny crack growing preferentially toward the nearest free surfaces [Colour figure can be viewed at [wileyonlinelibrary.com](http://wileyonlinelibrary.com)]

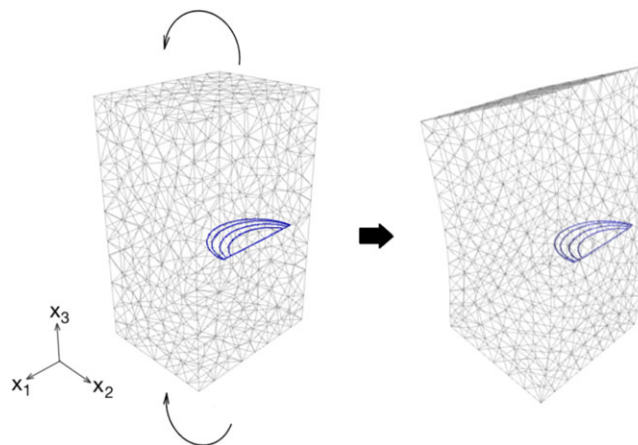
The crack, which initially has an axisymmetric shape, grows preferentially toward the closer free boundaries of the prism. This is due to the boundary correction (image stress contribution), which results in larger PK forces on crack segments closer to the free boundaries. The effect is an elongation of the crack into an elliptical shape with a semimajor axis  $a$  and a semiminor axis  $b$ . The difference between  $a$  and  $b$ , scaled by the maximum value of  $a$ , is shown in Figure 16B as the DCM simulation proceeds.

### 6.3 | Three-dimensional surface crack in a beam under imposed end rotation

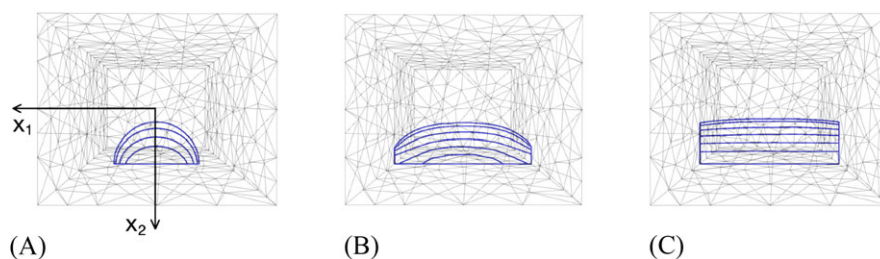
It is known that tensile loads typically result in unstable crack growth under both dead-load and fixed-grip conditions. However, stable crack growth can occur under certain bending conditions.<sup>39</sup> While constant applied bending loads will cause a crack to grow uncontrollably, fixed-grip bending loads (such as a fixed rotation at ends of a beam) can result in stable crack growth. By combining the use of level sets and the XFEM, Gravouil et al showed that a semicircular crack in a beam under a bending load will propagate through the beam completely once crack growth is initiated.<sup>40</sup> In contrast, the following example demonstrates stable growth of a semicircular crack in a beam ( $\mu = 18.5$  GPa,  $\nu = 0.27$ ,  $K_c = 1.25$  MPa $\sqrt{\text{m}}$ ) with fixed rotations applied to the ends, as shown in Figure 17. The beam has a width of 2.5 mm, a depth of 2 mm, and a height of 4 mm. A semicircular surface crack along the  $x_3 = 0$  plane with an initial radius of  $a_0 = 0.75$  mm is located centrally on the  $x_2 = 1$  mm face of the beam. The top and bottom beam faces are rotated symmetrically by 0.0025 radians about their central axes parallel to the  $x_1$  axis, such that tensile stresses are developed in the  $+x_2$  half of the beam.

Figure 18 shows the progression of the semicircular crack under the bending load. Note that the crack opening at the surface of the beam is represented by crack dislocation segments with the appropriate Burgers vectors. When the prescribed end rotations are applied to the beam, the crack quickly widens toward the lateral surfaces of the beam and then grows slowly toward the neutral axis. This behavior is consistent with the stress field in a beam under bending. According to the beam geometry and end conditions, the bending stress and crack shape should be symmetric across the  $x_1$ -plane. However, some asymmetry is observed in the crack shape as a result of the lack of symmetry in the mesh used for the simulation. Since the crack growth is governed by the PK force obtained from the stress along the leading dislocation, it follows that a slight deviation from the symmetric elastic field solution will result in crack growth that is somewhat asymmetric. For symmetric problems, this can be mitigated by using a symmetric mesh or by imposing symmetry conditions and only modeling a portion of the geometry.

If the edge crack continues to grow upon reaching the lateral faces of the beam, an “unzipping” of the beam occurs. This is modeled with the DCM method by confining the regions of the crack that intersect the lateral surfaces to move only along those surfaces. This unzipping is shown in Figures 18 and 19, which also show the displacement magnified by 100 at two cross sections of the beam—the midplane at  $x_1 = 0$  and a plane located at  $x_1 = 0.83$  mm. Plotting the crack opening component of the stress field ( $\sigma_{33}$ ) normalized by the shear modulus  $\mu$  reveals the stress relaxation associated



**FIGURE 17** Beam containing a semicircular surface crack with fixed rotations applied to the ends [Colour figure can be viewed at [wileyonlinelibrary.com](http://wileyonlinelibrary.com)]



**FIGURE 18** Dislocation array representing a semicircular crack for (A) initial crack shape, (B) crack as it unzips along sides of pillar, and (C) final crack shape [Colour figure can be viewed at [wileyonlinelibrary.com](http://wileyonlinelibrary.com)]

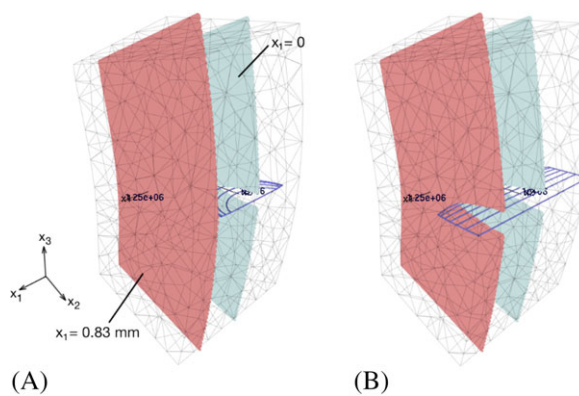


**FIGURE 19** Cross sections showing crack opening displacement  $\times 100$  for (A) initial crack state and (B) final crack state [Colour figure can be viewed at [wileyonlinelibrary.com](http://wileyonlinelibrary.com)]

with crack growth, as shown in Figure 20. Note that the relaxation is less dramatic at the midplane where the initial crack tip is close to the neutral axis as opposed to the relaxation at the plane at  $x_1 = 0.83$  mm, which is not initially intersected by the crack (see Figure 19).

Recall that virtual segments are used to alleviate the numerical difficulty of calculating the correction traction contribution of the boundary crack dislocations. The evolution of the virtual segments as the crack shape changes in this example, including when the crack sweeps around the corners of the beam, are shown in Figure 21.

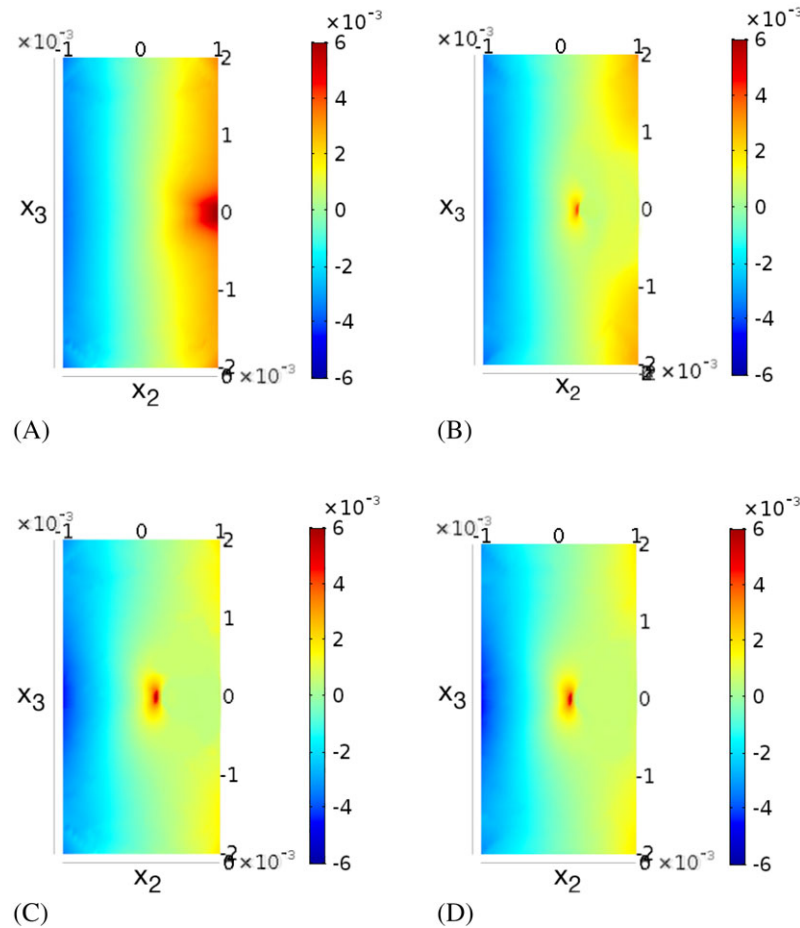


**FIGURE 20** Cross-sectional view of  $\sigma_{33}/\mu$  distribution for the initial crack shape at (A)  $x_1 = 0.83$  mm and (B) the midplane and for the final crack shape at (C)  $x_1 = 0.83$  mm and (D) the midplane

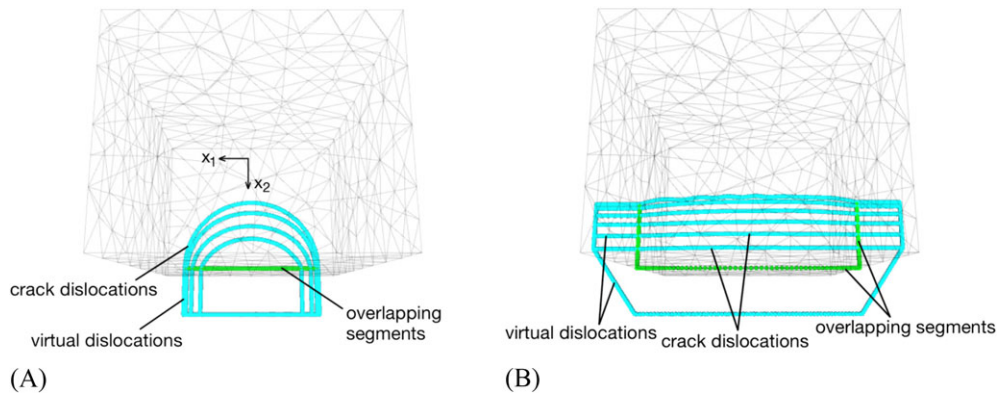


**FIGURE 21** Crack dislocations, virtual dislocations, and their overlapping boundary segments shown for (A) the initial crack shape and (B) the final crack shape [Colour figure can be viewed at [wileyonlinelibrary.com](http://wileyonlinelibrary.com)]

To demonstrate the mesh independence of the DCM method, the surface cracked beam example was repeated six times with increasingly fine mesh sizes used for the boundary correction problem. In Figure 22, the SIF at the center of the crack tip and the crack tip along the beam surface is plotted against the number of mesh elements used, showing clearly that the mesh has a minimal effect on the solution.



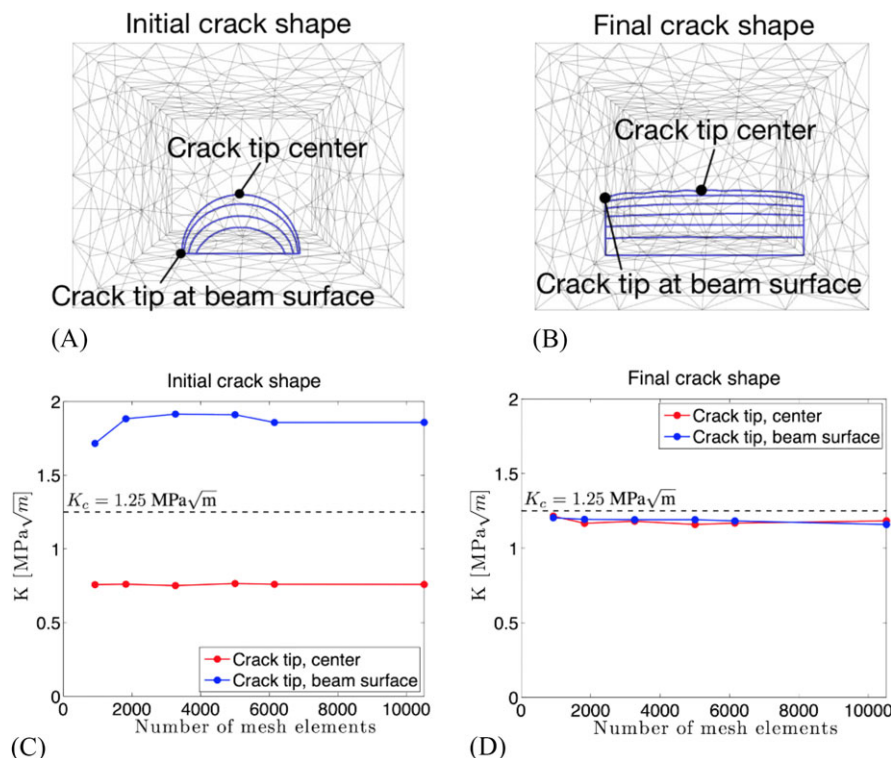


**FIGURE 22** Crack tip at the center and at the beam surface for (A) the initial crack shape and (B) the final crack shape, as well as (C) the initial stress and (D) final stress intensity factors at the center and surface crack tips vs the number of mesh elements

## 7 | SUMMARY AND CONCLUSIONS

The DCM method described herein successfully demonstrates the use of discrete dislocation arrays to model cracks. It has also been shown to address one of the major challenges faced in modeling 3D crack propagation, namely, the dependence of the crack field and path on the FEM mesh. The dislocation representation of a crack allows for an accurate computation of the near-tip elastic fields without requiring local mesh refinement. In addition, the effect of the free boundaries on a crack in a finite body can be accounted for by solving a boundary correction problem and superimposing the solution onto the infinite-medium solution of the crack dislocation array. Crack dislocations and the underlying mesh used in the correction problem can be independently selected. In contrast, methods such as the cohesive zone model require local mesh refinement to produce an accurate crack path, whereas other mesh-independent methods (eg, XFEM) require knowledge of the crack position relative to the underlying mesh in order to locally enrich nodal shape functions.

The accuracy of the DCM method has been verified through several benchmark problems. The DCM solutions for 2D mixed-mode cracks and for a 3D penny-shaped crack have been shown to be in excellent agreement with established solutions using only a small number of dislocations. Implementation of the boundary correction procedure has been demonstrated, with the resulting image forces increasing the SIF calculated along the leading dislocation. We have also applied the equations of motion formulated in this work to model quasi-static crack growth and shown stable crack propagation with an example of a beam with a semicircular surface crack subjected to prescribed rotations at its ends. The advancement of the crack front is shown to be nonuniform and that the crack shape adjusts to its proximity to the nearest boundaries. At the midsection of the crack, the propagation speed is slow, whereas at the flanks, the front propagates at a faster rate. This results in straightening the semicircular crack so as to effectively accommodate the imposed rotation on the prismatic beam.

In this work, we have focused on a subset of problems in the realm of fracture mechanics, namely, quasi-static growth of 3D planar cracks in elastic materials. Having verified its application in solving these types of problems, we now comment on possible future improvements to expand the capabilities of the DCM method. Here, we have established some of the groundwork necessary for combining crack dislocations with crystal dislocations for cases involving elastic-plastic



fracture by introducing the equations of motion for a system containing both types of dislocations. Efforts to include their mutual interaction are currently in progress. Problems involving nonplanar cracks will require the implementation of additional features. For example, a criteria for determining the direction of crack tip advancement must be introduced, and the surface swept by the leading crack tip dislocation must be tracked and trailing dislocations confined to this surface, as demonstrated in the work of Ghoniem and Huang.<sup>5</sup> With regard to modeling dynamic crack growth, it may be possible to implement the elastodynamic fields of fast moving dislocations presented by Cui et al to extend the capabilities of the DCM method.<sup>10</sup>

In summary, the following novel features have been introduced in this work.

1. The conditions for the simultaneous equilibrium and mutual interaction between Volterra dislocation arrays under general loading in 2D and 3D are demonstrated.
2. The insensitivity of crack growth and shape to the underlying mesh in finite domains is established, and the reasons for such insensitivity are uncovered.
3. A general formula for the J-integral and its relationship to the PK force is derived for 3D cracks.
4. A variational formulation of the equation of motion governing the crack tip during crack growth is derived, where the motion of cracks and crystal dislocations are coupled.
5. A general method for the selection of Volterra dislocation Burgers vector and orientation is established.
6. Quasi-static growth of both surface and bulk cracks in 3D geometry is demonstrated in finite domains.
7. Conditions for stable versus unstable crack growth are shown under displacement and load control, respectively.

## ACKNOWLEDGEMENTS

This work was partially supported by the Air Force Office of Scientific Research (AFOSR) under Award No. FA9550-16-1-0444 with UCLA and by the United States Department of Energy under Award No. DE-SC0018410 with UCLA. Giacomo Po acknowledges support from the National Science Foundation, Division of Civil, Mechanical and Manufacturing Innovation (CMMI), under Award No. 1563427 with UCLA.

## ORCID

A. Sheng  <http://orcid.org/0000-0003-3375-0361>

## REFERENCES

1. Eshelby JD, Frank FC, Nabarro FRN. XLI: the equilibrium of linear arrays of dislocations. *Lond Edinb Dublin Philos Mag J Sci*. 1951;42(327):351-364.
2. Weertman J. *Dislocation-based Fracture Mechanics*. Singapore: World Scientific Publishing Company; 1996.
3. Ghoniem NM, Tong S-H, Sun LZ. Parametric dislocation dynamics: a thermodynamics-based approach to investigations of mesoscopic plastic deformation. *Phys Rev B*. 2000;61(2):913.
4. Po G, Ghoniem NM. A variational formulation of constrained dislocation dynamics coupled with heat and vacancy diffusion. *J Mech Phys Solids*. 2014;66:103-116.
5. Ghoniem NM, Huang J. The elastic field of general-shape 3-D cracks. *Philos Mag*. 2006;86(27):4195-4212.
6. Takahashi A, Ghoniem NM. Fracture mechanics of propagating 3-D fatigue cracks with parametric dislocations. *Philos Mag*. 2013;93(20):2662-2679.
7. Eshelby JD. The elastic field of a crack extending non-uniformly under general anti-plane loading. *J Mech Phys Solids*. 1969;17(3):177-199.
8. Xu X-P, Needleman A. Numerical simulations of fast crack growth in brittle solids. *J Mech Phys Solids*. 1994;42(9):1397-1434.
9. Réthoré J, Gravouil A, Combescure A. An energy-conserving scheme for dynamic crack growth using the extended finite element method. *Int J Numer Methods Eng*. 2005;63(5):631-659.
10. Cui Y, Po G, Pellegrini Y-P, Lazar M, Ghoniem N. Elastodynamics of 3-Dimensional dislocations under shock loading. *J Mech Phys Solids*. 2018. In preparation (to be submitted).
11. Song J-H, Wang H, Belytschko T. A comparative study on finite element methods for dynamic fracture. *Comput Mech*. 2008;42(2):239-250.
12. Belytschko T, Krongauz Y, Organ D, Fleming M, Krysl P. Meshless methods: an overview and recent developments. *Comput Methods Appl Mech Eng*. 1996;139(1-4):3-47.
13. Nguyen VP, Rabczuk T, Bordas S, Duflot M. Meshless methods: a review and computer implementation aspects. *Math Comput Simul*. 2008;79(3):763-813.

14. Belytschko T, Lu YY, Gu L. Element-free Galerkin methods. *Int J Numer Methods Eng*. 1994;37(2):229-256.
15. Belytschko T, Gu L, Lu YY. Fracture and crack growth by element free Galerkin methods. *Model Simul Mater Sci Eng*. 1994;2(3A):519.
16. Sukumar N, Moran B, Black T, Belytschko T. An element-free Galerkin method for three-dimensional fracture mechanics. *Comput Mech*. 1997;20(1-2):170-175.
17. Krysl P, Belytschko T. The element free Galerkin method for dynamic propagation of arbitrary 3-D cracks. *Int J Numer Methods Eng*. 1999;44(6):767-800.
18. Rabczuk T, Belytschko T. Cracking particles: a simplified meshfree method for arbitrary evolving cracks. *Int J Numer Methods Eng*. 2004;61(13):2316-2343.
19. Moës N, Dolbow J, Belytschko T. A finite element method for crack growth without remeshing. *Int J Numer Methods Eng*. 1999;46(1):131-150.
20. Strouboulis T, Babuška I, Copps K. The design and analysis of the generalized finite element method. *Comput Methods Appl Mech Eng*. 2000;181(1-3):43-69.
21. Rabczuk T. Computational methods for fracture in brittle and quasi-brittle solids: state-of-the-art review and future perspectives. *ISRN Appl Math*. 2013;2013.
22. Duarte CA, Babuška I, Oden JT. Generalized finite element methods for three-dimensional structural mechanics problems. *Comput Struct*. 2000;77(2):215-232.
23. Belytschko T, Gracie R, Ventura G. A review of extended/generalized finite element methods for material modeling. *Model Simul Mater Sci Eng*. 2009;17(4):043001.
24. Fries T-P, Belytschko T. The extended/generalized finite element method: an overview of the method and its applications. *Int J Numer Methods Eng*. 2010;84(3):253-304.
25. Bellet J, Dolbow JE. A note on enrichment functions for modelling crack nucleation. *Commun Numer Methods Eng*. 2003;19(12):921-932.
26. Rannou J, Gravouil A, Baïetto-Dubourg M-C. A local multigrid X-FEM strategy for 3-D crack propagation. *Int J Numer Methods Eng*. 2009;77(4):581-600.
27. Gracie R, Belytschko T. Concurrently coupled atomistic and XFEM models for dislocations and cracks. *Int J Numer Methods Eng*. 2009;78(3):354-378.
28. Eshelby JD. The force on an elastic singularity. *Phil Trans R Soc Lond A Math Phys Eng Sci*. 1951;244(877):87-112.
29. Hirth JP, Lothe J. *Theory of Dislocations*. Malabar, FL: Krieger Publishing Company; 1982.
30. Ghoniem NM, Sun LZ. Fast-sum method for the elastic field of three-dimensional dislocation ensembles. *Phys Rev B*. 1999;60(1):128.
31. Van der Giessen E, Needleman A. Discrete dislocation plasticity: a simple planar model. *Model Simul Mater Sci Eng*. 1995;3(5):689.
32. Po G, Mohamed MS, Crosby T, Erel C, El-Azab A, Ghoniem N. Recent progress in discrete dislocation dynamics and its applications to micro plasticity. *JOM*. 2014;66(10):2108-2120.
33. Belytschko T, Gracie R. On XFEM applications to dislocations and interfaces. *Int J Plast*. 2007;23(10-11):1721-1738.
34. Mura T. *Micromechanics of Defects in Solids*. Dordrecht, The Netherlands: Martinus Nijhoff Publishers; 1987.
35. Slattey JC, Sagis L, Oh E-S. *Interfacial Transport Phenomena*. New York, NY: Springer Science+Business Media; 2007.
36. Tada H, Paris PC, Irwin GR. *The Analysis of Cracks Handbook*. New York, NY: ASME Press; 2000.
37. Rooke DP, Cartwright DJ. *Compendium of Stress Intensity Factors*. Procurement Executive, Ministry of Defence. London, UK: Her Majesty's Stationery Office; 1976.
38. Hammouda MMI, Fayed AS, Sallam HEM. Stress intensity factors of a central slant crack with frictional surfaces in plates with biaxial loading. *Int J Fract*. 2004;129(2):141-148.
39. Cotterell B, Mai Y-W. *Fracture Mechanics of Cementitious Materials*. Boca Raton, FL: CRC Press; 1995.
40. Gravouil A, Moës N, Belytschko T. Non-planar 3D crack growth by the extended finite element and level sets—Part II: level set update. *Int J Numer Methods Eng*. 2002;53(11):2569-2586.

**How to cite this article:** Sheng A, Ghoniem NM, Crosby T, Po G. A mesh-independent method for planar three-dimensional crack growth in finite domains. *Int J Numer Methods Eng*. 2019;117:38–62. <https://doi.org/10.1002/nme.5946>